Electronic conduction properties of indium tin oxide: single-particle and many-body transport

2014 J. Phys.: Condens. Matter 26 343201

(http://iopscience.iop.org/0953-8984/26/34/343201)

IOP Publishing Journal of Physics: Condensed Matter
J. Phys.: Condens. Matter **26** (2014) 343201 (21pp) doi:10.1088/0953-8984/26/34/343201

Topical Review

Electronic conduction properties of indium tin oxide: single-particle and many-body transport

Juhn-Jong Lin[1] **and Zhi-Qing Li**[2]

[1] NCTU-RIKEN Joint Research Laboratory, Institute of Physics and Department of Electrophysics, National Chiao Tung University, Hsinchu 30010, Taiwan
[2] Tianjin Key Laboratory of Low Dimensional Materials Physics and Preparing Technology, Department of Physics, Tianjin University, Tianjin 300072, People's Republic of China

E-mail: jjlin@mail.nctu.edu.tw

Received 1 April 2014, revised 29 June 2014
Accepted for publication 1 July 2014
Published 8 August 2014

Abstract

Indium tin oxide (Sn-doped $In_2O_{3-\delta}$ or ITO) is a very interesting and technologically important transparent conducting oxide. This class of material has been extensively investigated for decades, with research efforts mostly focusing on the application aspects. The fundamental issues of the electronic conduction properties of ITO from room temperature down to liquid-helium temperatures have rarely been addressed thus far. Studies of the electrical-transport properties over a wide range of temperature are essential to unravelling the underlying electronic dynamics and microscopic electronic parameters. In this topical review, we show that one can learn rich physics in ITO material, including the semi-classical Boltzmann transport, the quantum-interference electron transport, as well as the many-body Coulomb electron–electron interaction effects in the presence of disorder and inhomogeneity (granularity). To fully reveal the numerous avenues and unique opportunities that the ITO material has provided for fundamental condensed matter physics research, we demonstrate a variety of charge transport properties in different forms of ITO structures, including homogeneous polycrystalline thin and thick films, homogeneous single-crystalline nanowires and inhomogeneous ultrathin films. In this manner, we not only address new physics phenomena that can arise in ITO but also illustrate the versatility of the stable ITO material forms for potential technological applications. We emphasize that, microscopically, the novel and rich electronic conduction properties of ITO originate from the inherited robust free-electron-like energy bandstructure and low-carrier concentration (as compared with that in typical metals) characteristics of this class of material. Furthermore, a low carrier concentration leads to slow electron–phonon relaxation, which in turn causes the experimentally observed (i) a small residual resistance ratio, (ii) a linear electron diffusion thermoelectric power in a wide temperature range 1–300 K and (iii) a weak electron dephasing rate. We focus our discussion on the metallic-like ITO material.

Keywords: indium tin oxide, transparent conducting oxides, electronic conduction properties, Boltzmann transport, localization, mesoscopic physics, granular systems

(Some figures may appear in colour only in the online journal)

1. Introduction

Transparent conducting oxides (TCOs) constitute an appearing and unique class of materials that simultaneously possess high electrical conductivity, σ and high optical transparency at the visible frequencies [1–3]. These combined electrical and optical properties render the TCOs to be widely used, for example, as transparent electrodes in numerous optoelectronic devices, such as flat panel displays, photovoltaic electrochromics, solar cells, energy-efficient windows and resistive touch panes [3–6]. Currently, the major industrial TCO films are made of indium tin oxide (Sn-doped $In_2O_{3-\delta}$ or so-called ITO), F-doped tin oxide and group III elements doped zinc oxide. Among them, the ITO films are probably the most widely used TCOs, owing to the ITO's readiness for fabrication and patterning as well as their high quality and reliability implemented in commercial products.

On the fundamental research side, our current understanding of the origins for the combined properties of high electrical conductivity and high optical transparency is based on both theoretical and experimental studies [7–33]. The electronic energy bandstructure of ITO has been theoretically calculated by several authors [26–29]. It is now known that the bottom of the conduction band of the parent In_2O_3 is mainly derived from the hybridization of the In 5*s* electronic states with the O 2*s* states. The energy-momentum dispersion near the bottom of the conduction band reveals a parabolic character, manifesting the nature of *s*-like electronic states (see a schematic in figure 1). The Fermi level lies in the middle of the conduction and valence bands, rendering In_2O_3 a wide-band-gap insulator. Upon doping, the Sn 5*s* electrons contribute significantly to the electronic states around the bottom of the conduction band, causing the Fermi level to shift upward into the conduction band. Meanwhile, the shape of the conduction band at the Fermi level faithfully retains the intrinsic parabolic character. This unique material property makes ITO a highly degenerate n-type semiconductor or, alternatively, a low-carrier-concentration metal. As a consequence of the *s*-like parabolic energy bandstructure, the electronic conduction properties of this class of material demonstrate marked *free-carrier-like* characteristics. The charge transport properties of ITO can thus be quantitatively described by those simple models formulated basing upon a free electron Fermi gas. Indeed, the levels of close quantitative agreement between theoretical calculations and experimental measurements obtained for ITO are not achievable even for alkali (Li, Na, K) and noble (Cu, Ag, Au) metals, as we shall present in this topical review.

In practice, the conduction electron concentration, n, in optimally doped ITO (corresponding to approximately 8 at.% of Sn doping) can reach a level as high as $n \approx 10^{20}$–10^{21} cm^{-3} [34, 35]. This level of n is *two to three orders of magnitude lower* than that ($\approx 10^{22}$–10^{23} cm^{-3} [36]) in typical metals. The room temperature resistivity can be as low as $\rho(300\,\mathrm{K}) \approx 150\,\mu\Omega\,\mathrm{cm}$ (see table 1). This magnitude is comparable with that of the technologically important titanium–aluminium alloys [37, 38]. In terms of the optical properties, the typical plasma frequency is $\omega_p \simeq 0.7$–$1\,\mathrm{eV}$ [8], while the typical energy band gap is $E_g \simeq 3.7$–$4.0\,\mathrm{eV}$. Hence, optimally doped ITO possesses a high optical transparency which exceeds 90% transmittance at the visible light frequencies [39, 40]. A value of $\omega_p \simeq 1\,\mathrm{eV}$ corresponds to a radiation frequency of $f_p = \omega_p/2\pi \simeq 2.4 \times 10^{14}\,\mathrm{Hz}$, which is approximately one fifth of the visible light frequency and roughly one fiftieth of the plasma frequency of a typical metal. For optoelectronic applications, on one hand, one would like to dope ITO with a Sn level as high as technologically feasible in order to obtain a high electrical conductivity σ. On the other hand, since $\omega_p \propto \sqrt{n}$, one has to keep n sufficiently low such that the visible light can propagate through the ITO structure.

Owing to their technological importance, it is natural that there already exist in the literature a number of review articles on the ITO as well as TCO materials [2, 4, 41–51]. The early studies up to 1982, covering the deposition methods, crystal structures, scattering mechanisms of conduction electrons and the optical properties of In_2O_3, SnO_2 and ITO, were reviewed by Jarzębski [2]. Hamberg and Granqvist discussed the optical properties of ITO films fabricated by the reactive electron-gun evaporation onto heated glass substrates [42]. The development up to 2000 on the various aspects of utilizing TCOs was summarized in reports considering, for example, characterizations [48], applications and processing [43], criteria for choosing transparent conductors [47], new n- and p-type TCOs [44, 45] and the chemical and thin-film strategies for new TCOs [46]. The recent progresses in new TCO materials and TCOs based devices were discussed in [49] and [50]. King and Veal recently surveyed the current theoretical understanding of the effects of defects, impurities and surface states on the electrical conduction in TCOs [51].

In this topical review, we stress the free-electron-like energy bandstructure and the low-n features (as compared with typical metals) of the ITO material. These inherited intrinsic electronic characteristics make ITO a model system which is ideal for not only revealing the semi-classical Boltzmann transport behaviours (section 2) but also studying new physics such as the quantum-interference weak-localization (WL) effect and the universal conduction fluctuations (UCFs) in miniature structures (section 3). The responsible electron dephasing (electron–electron scattering, electron–phonon scattering and spin–orbit scattering) processes are discussed. Furthermore, we show that this class of material provides a very useful platform for experimentally testing the recent theories of *granular metals* [52–57]. In the last case, ultrathin ITO films can be intentionally made to be slightly inhomogeneous or granular, while the coupling between neighbouring grains remains sufficiently strong so that the system retains global metallic-like conduction (section 4). To illustrate the unique and numerous avenues provided by ITO for the studies of the aforementioned semi-classical versus quantum electron transport, as well as homogeneous versus inhomogeneous charge transport, we cover polycrystalline (ultra)thin and thick ITO films and single-crystalline ITO nanowires in this topical review. We demonstrate that high-quality ITO structures can indeed be readily fabricated into various forms which, apart from being powerful for addressing fundamental electronic conduction properties, may be useful for potential technological applications. Furthermore, owing

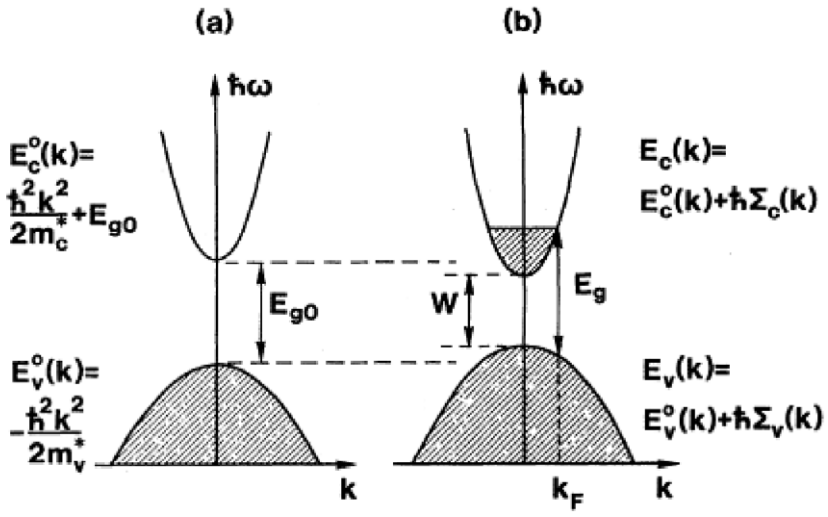

Figure 1. Schematic energy bandstructure showing the top of the valence band and the bottom of the conduction band for (*a*) In_2O_3 and (*b*) Sn-doped In_2O_3 ($In_{2-x}Sn_xO_{3-\delta}$). This figure was reproduced with permission from [7]. Copyright 1984 by the American Physical Society.

to the similarities in electronic bandstructure between ITO and other TCO materials [3], we expect that the electronic processes and mechanisms discussed in this topical review should be useful for understanding and interpreting the results obtained on general TCOs.

We do not cover insulating or amorphous ITO materials in this topical review, where the electronic conduction processes can be due to thermally excited hopping [58–62]. In addition to the conventional Mott [63] and Efros-Shklovskii [64] hopping conduction mechanisms in homogeneous strongly disordered systems, electronic conduction due to the thermal charging effect [65] and, more recently, the variable-range-hopping process [66] in inhomogeneous (granular) systems have been discussed in literature. On the other hand, the possible occurrence of superconductivity in ITO has been explored in [67–70].

2. Free-electron-like Boltzmann transport: homogeneous indium tin oxide films and nanowires

The electrical-transport properties of ITO films have extensively been discussed in the literature. However, previous studies have mainly concentrated on the influences of deposition methods and conditions on the $\rho(300\,\mathrm{K})$ values. While those studies have provided useful information for improving the fabrication of high-quality ITO films, they did not deal with the underlying electronic conduction processes in ITO. In section 2.1, we first briefly summarize the theoretical calculations of the electronic energy bandstructure of ITO and explain why this class of material behaves like a highly degenerate semiconductor or a low-*n* metal. In section 2.2, we discuss the overall temperature behaviour of resistivity $\rho(T)$ in ITO and show that $\rho(T)$ can be well described by the standard Boltzmann transport equation in a wide temperature range. In section 2.3, we demonstrate that the thermoelectric power (Seebeck coefficient, or thermopower), $S(T)$, in ITO follows an approximately linear temperature dependence in the wide temperature range from 1 K up to well above room temperature. This *linear thermoelectric power* originates from the diffusion of electrons in the presence of a temperature gradient and provides a powerful, direct manifestation of the robust free-carrier-like characteristic of ITO. The reason why the phonon-drag contribution to thermoelectric power in ITO is absent is heuristically discussed.

2.1. Free-carrier-like bandstructure and relevant electronic parameters

2.1.1. Electronic energy bandstructure. Since the electronic energy bandstructure plays a key role in governing the charge transport properties of a given material, we first discuss the electronic bandstructure of ITO. Based on their x-ray photoemission spectroscopy studies, Fan and Goodenough [71] first suggested a schematic energy band model for the undoped and Sn-doped In_2O_3 in 1977. A heuristic energy-band model for ITO was proposed by Hamberg *et al* [7] in 1984. In their heuristic model (shown in figure 1), the bottom (top) of the conduction (valence) band of In_2O_3 was taken to be parabolic. They further proposed that the shapes of the conduction band and the valence band remained unchanged upon Sn doping. This simple bandstructure model is qualitatively in line with that obtained by later theoretical calculations [26–29].

The first *ab initio* bandstructure calculations for the ITO material were carried out by Odaka *et al* [26] and Mryasov and Freeman [27] in 2001. Later on, Medvedeva [28] calculated the bandstructure of In_2O_3 and Medvedeva and Hettiarachchi [29] calculated the bandstructure of 6.25 at.% Sn-doped In_2O_3. Figures 2(*a*) and (*b*), respectively, show the electronic bandstructures of stoichiometric In_2O_3 and 6.25 at.% Sn-doped In_2O_3 obtained in [29]. For In_2O_3, the conduction band exhibits a free-electron-like, parabolic characteristic around the Γ point, where the bottom of the conduction band originates from the hybridization of In 5*s* and O 2*s* electronic states. Medvedeva and Hettiarachchi found that the effective electron mass, m^*, near the Γ point is nearly

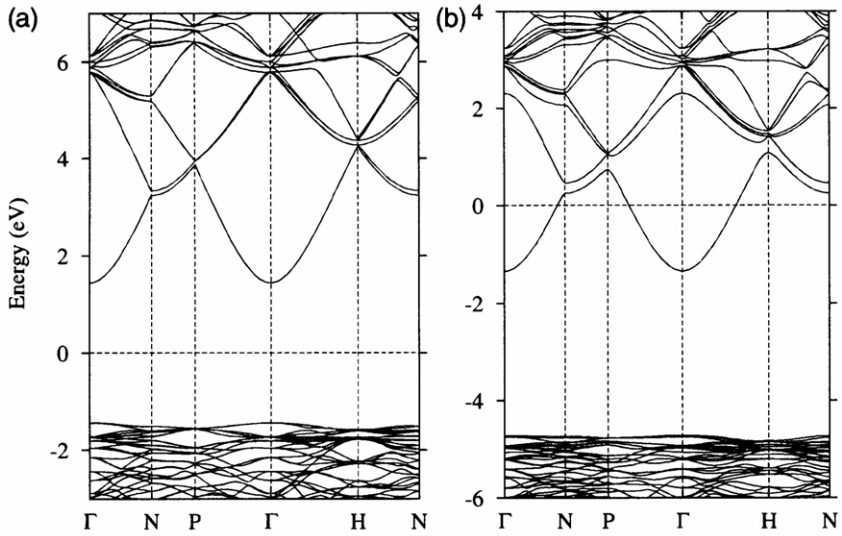

Figure 2. Electronic energy bandstructure of (*a*) undoped In_2O_3 and (*b*) 6.25 at.% Sn-doped In_2O_3. In (*b*), a 6.25 at.% doping level corresponds to a single Sn atom substituting for one of the 16 In atoms in the In_2O_3 supercell. Note the inherent free-electron-like energy-momentum dispersion at the Fermi level. This figure was reproduced with permission from [29]. Copyright 2010 by the American Physical Society.

isotropic. Similar theoretical results were obtained shortly after by Fuchs and Bechstedt [72] and Karazhanov *et al* [12].

Upon Sn doping, the Sn 5*s* states further hybridize with the In 5*s* and O 2*s* states to form the bottom of the conduction band. Furthermore, the Fermi level in ITO shifts upward into the conduction band, leading to the bandstructure depicted in figure 2(*b*). Theoretical calculations indicate that the Sn 5*s* states contribute nearly one fourth of the total electronic density of states at the Fermi level, $N(E_F)$, while the In 5*s* and O 2*s* states contribute the rest. At this particular doping level, the *s*-like symmetry of the original bandstructure around the Fermi level in the parent In_2O_3 is essentially unaltered. Thus, the conduction electrons at the Fermi level in ITO possess strong free-carrier-like features. Meanwhile, Fuchs and Bechstedt [72] found that the average effective electron mass increases slightly with increasing carrier concentration n. At a level of $n \simeq 10^{20}\,\mathrm{cm}^{-3}$, they obtained a value $m^* \simeq 0.3\,m_e$, where m_e is the free-electron mass. Their result agreed with that derived from optical measurements of the Drude term to free carriers [7].

In brief, the combined electronic bandstructure characteristics of a wide energy gap, a small m^* and in particular a low n as well as a free-carrier-like dispersion at E_F, are the crucial ingredients to make ITO, on one hand, possess high electrical conductivity while, on the other hand, reveal high optical transparency.

2.1.2. Relevant electronic parameters. Experimentally, a reliable method to check the metal-like energy bandstructure of a material is to examine the temperature T dependence of n. For a metal or a highly degenerate semiconductor, n does not vary with T. Figure 3 shows the variation of n with temperature for a few as-deposited (before annealing) and annealed ITO films studied by Kikuchi *et al* [73]. It is clear

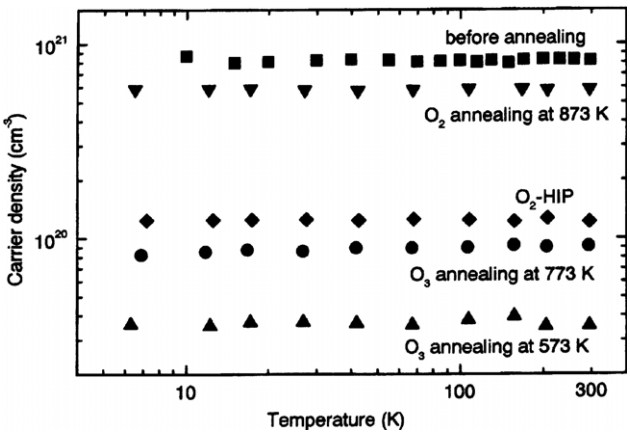

Figure 3. Carrier concentration as a function of temperature for as-prepared (before annealing) and annealed ITO films. O_2-HIP denotes annealing in an O_2 atmosphere and O_3 denotes annealing in an O_3 atmosphere. This figure was reproduced with permission from [73]. Copyright 2000 by Elsevier.

that n remains constant in a wide T range from liquid-helium temperatures up to 300 K. In the as-deposited sample, the n value approaches $\sim 1 \times 10^{21}\,\mathrm{cm}^{-3}$. Temperature independent n in the ITO material has been reported by a number of groups [61, 74–76].

For the convenience of the discussion of charge transport properties in ITO in this topical review, we would like to estimate the values of relevant electronic parameters. Consider a high-quality ITO sample having a value of $\rho(300\,\mathrm{K}) \simeq 150\,\mu\Omega\,\mathrm{cm}$, a carrier concentration $n \simeq 1 \times 10^{21}\,\mathrm{cm}^{-3}$ and an effective mass $m^* \simeq 0.35\,m_e$. Applying the free-electron model, we obtain the Fermi wavenumber $k_F = (3\pi^2 n)^{1/3} \simeq 3.1 \times 10^9\,\mathrm{m}^{-1}$, the Fermi velocity $v_F = \hbar k_F/m^* \simeq 1.0 \times 10^6\,\mathrm{m\,s}^{-1}$ and the Fermi energy $E_F = \hbar^2 k_F^2/(2m^*) \simeq 1.0\,\mathrm{eV}$. The electron mean free

Table 1. Representative values of room temperature resistivity ρ and carrier concentration n for ITO films fabricated by different deposition methods.

Fabrication method	ρ ($\mu\Omega$ cm)	n (10^{20} cm^{-3})	References
Vacuum evaporation	~150–15 000	~5	[35, 61, 77–79]
Magnetron sputtering	~100–400	~10	[80–83]
Chemical vapour deposition	~150–500	~10	[84–86]
Sol-gel	~600–4000	~1	[87–90]
Spray pyrolysis	~900–5000	~1	[91–93]

time is $\tau = m^*/(ne^2\rho) \simeq 8.3 \times 10^{-15}$ s, corresponding to the electron mean free path $l = v_F\tau \simeq 8.3$ nm. The electron diffusion constant $D = v_F l/3 \simeq 28\,\text{cm}^2\,\text{s}^{-1}$. Thus, the dimensionless product $k_F l \simeq 26$. Note that $k_F l$ is an important physical quantity which characterizes the degree of disorder in a conductor. A $k_F l$ value of order a few tens indicates that high-quality ITO is a weakly disordered metal and should thus be rich in quantum-interference transport phenomena.

In practice, the ρ and n values in ITO films can vary widely with the deposition methods and conditions, Sn doping levels and the post thermal treatment conditions. In table 1, we list some representative values for ITO films prepared by different techniques. This table indicates that those ITO films fabricated by the DC magnetron sputtering method possess relatively high (low) n (ρ) values. Since the films thus prepared are compact and they adhere well to the substrate surface, this low-cost technique is thus the most widely used ITO deposition method in the industrial production nowadays. Recently, researchers have also carried out molecular-beam-epitaxial growth studies of ITO structures [94, 95], but the crystal quality obtained was not as high as that previously achieved in the epitaxial films grown by a pulsed-laser deposition technique [96]. We mention in passing that, apart from the bulk properties [97, 98], the effect on electronic processes of the surface states due to oxygen vacancies in undoped $In_2O_{3-\delta}$ [32] as well as doped TCOs [30, 31, 51] has recently drawn theoretical and experimental attention.

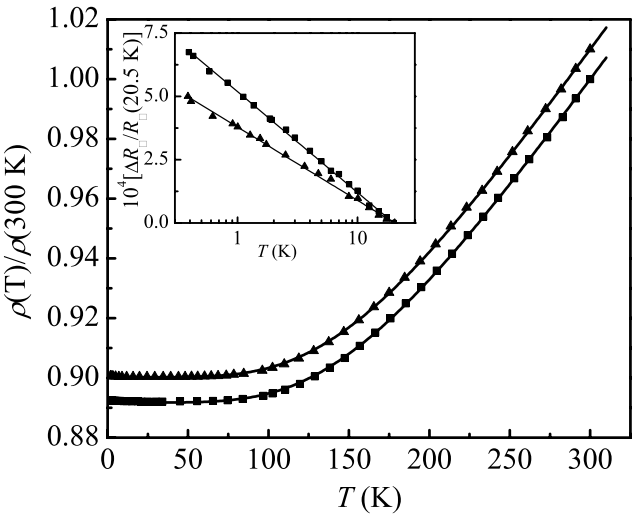

Figure 4. Normalized resistivity, $\rho(T)/\rho(300\,\text{K})$, as a function of temperature for a 125 nm (squares) and a 240 nm (triangles) thick ITO films. The symbols are the experimental data and the solid curves are the theoretical predictions of equation (1). For clarity, the data for the 240 nm thick film has been shifted up by 0.01. Inset: normalized sheet resistance, $\Delta R_\square(T)/R_\square = [R_\square(T) - R_\square(20.5\,\text{K})]/R_\square(20.5\,\text{K})$, as a function of the logarithm of temperature for these two films below 25 K. The straight solid lines are least-squares fits to the theoretical predictions of 2D WL and EEI effects. This figure was reproduced with permission from [99]. Copyright 2004 by the American Institute of Physics.

2.2. Temperature behaviour of electrical resistivity

The temperature dependence of resistivity $\rho(T)$ from 300 K down to liquid-helium temperatures provides key information for the understanding of the electrical conduction processes in a conductor. Li and Lin [99] have measured $\rho(T)$ between 0.4 and 300 K in a number of 125 and 240 nm thick polycrystalline ITO films prepared by the standard RF sputtering deposition method. Their films had relatively low values of $\rho(300\,\text{K}) \simeq 200\,\mu\Omega\,\text{cm}$. Their results are shown in figure 4. Li and Lin found that the $\rho(T)$ data between ~25 and 300 K can be well described by the Bloch–Grüneisen formula

$$\rho = \rho_e + \rho_{e\text{–ph}}(T) = \rho_e + \beta T\left(\frac{T}{\theta_D}\right)^4 \int_0^{\theta_D/T} \frac{x^5 dx}{(e^x - 1)(1 - e^x)}, \quad (1)$$

where ρ_e is a residual resistivity, β is an electron–phonon (e–ph) coupling constant and θ_D is the Debye temperature. The solid curves in the main panel of figure 4 are the theoretical predications of equation (1). This figure demonstrates that ITO is a metal, with ρ decreasing with decreasing temperature (or, a positive temperature coefficient of resistivity, i.e. $(1/\rho)(d\rho/dT) > 0$). In particular, the temperature dependence of $\rho(T)$ can be well described by the standard Boltzmann transport equation.

The first term on the right hand side of equation (1) originates from the elastic scattering of electrons with defects. The second term originates from the inelastic scattering of electrons with lattice vibrations (phonons). Using the Drude formula $\sigma = ne^2\tau/m^*$, one rewrites $\rho = (m^*/ne^2)(1/\tau_e + 1/\tau_{e\text{–ph}}) = \rho_e + \rho_{e\text{–ph}}(T)$, where e is the electronic charge, τ_e is the electron elastic mean free time and $\tau_{e\text{–ph}}$ is the e–ph relaxation time. From figure 4, one finds a small resistivity ratio $\rho(300\,\text{K})/\rho(25\,\text{K}) \simeq 1.1$, corresponding to the ratio of scattering rates $1/\tau_{e\text{–ph}} \simeq 0.1(1/\tau_e)$. This observation explicitly suggests that the e–ph relaxation in the ITO material is *weak* and hence the contribution of the e–ph scattering to $\rho(300\,\text{K})$ is only approximately one tenth of that of the electron elastic scattering with imperfections. A slow e–ph relaxation rate is a general intrinsic property of low-n conductors, see

below for further discussion[3]. The presence a moderate level of disorder in ITO films result in significant quantum-interference weak-localization (WL) and electron–electron interaction (EEI) effects at low temperatures. These two effects cause small corrections to the residual resistivity, which increase with reducing temperature. Close inspection of the inset of figure 4 indicates a well-defined, logarithmic temperature dependent resistivity rise below ~ 25 K. The two-dimensional (2D) WL and EEI effects will be discussed in section 3.

In addition to comparatively thick films, present-day RF sputtering deposition technology has advanced such that relatively thin films can be made metallic. In a recent study, Lin *et al* [103] found that the temperature dependence of $\rho(T)$ below 300 K for 15 nm thick polycrystalline ITO films can also be described by the Bloch–Grüneisen formula. However, the $\rho(T)$ curve reaches a minimum around 150 K. At lower temperatures, $\rho(T)$ increases with decreasing temperature, signifying much more pronounced 2D WL and EEI effects than in thicker films (figure 4).

The temperature dependence of resistivity in *single-crystalline* ITO nanowire has been investigated by Chiu *et al* [69]. They measured individual ITO nanowires from 300 K down to 1.5 K employing an electron-beam lithographic four-probe configuration. Figure 5 shows a plot of the normalized resistivity, $\rho(T)/\rho(300\,\mathrm{K})$, as a function of temperature for four ITO nanowires. The solid curves are the theoretical predications of equation (1), indicating that the experimental $\rho(T)$ data can be well described by the Bloch–Grüneisen formula. However, it is surprising that, in the wide temperature range 1–300 K, the resistivity drops by no more than ~20%, even though these nanowires are single-crystalline. This observation strongly suggests that these nanowires must contain high levels of point defects which are not detectable by the high-resolution transmission electron microscopy studies [69]. It is worth noting that these nanowires are three-dimensional (3D) with respect to the Boltzmann transport, because the electron elastic mean free paths $\ell_e = v_F\tau_e \approx$ 5–11 nm are smaller than the nanowire diameters $d \approx$ 110–220 nm. On the other hand, the nanowires are one-dimensional (1D) with respect to the WL effect and the UCF phenomena, because the electron dephasing length $L_\varphi = \sqrt{D\tau_\varphi} > d$ at low temperatures, where τ_φ is the electron dephasing time (see section 3).

From least-squares fits of the measured $\rho(T)$ to equation (1), several groups have obtained a comparatively high Debye temperature of $\theta_D \sim 1000$ K in ITO thick films [61, 99], thin films [103] and nanowires [69]. This magnitude of θ_D is much higher than those (~200–400 K [36]) in typical metals[4].

[3] For comparison, we note that in typical disordered metals, a measured small residual resistivity ratio $\rho(300\,\mathrm{K})/\rho(4\,\mathrm{K})$ is usually due to a large elastic electron scattering rate $1/\tau_e$, because the e–ph relaxation is considerably fast in typical metals, see for example [100–102].

[4] In applying equation (1) to describe the $\rho(T)$ data in figures 4 and 5, we have focused on the temperature regime below room temperature. At room temperature and above, the interaction of electrons with polar optical phonons is strong. By taking into consideration electron–polar optical phonon interaction, Preissler *et al* [104] obtained a value of $\theta_D \simeq 700$ K from studies of Hall mobility in In_2O_3. These studies suggest a high Debye temperature in the In_2O_3 based material.

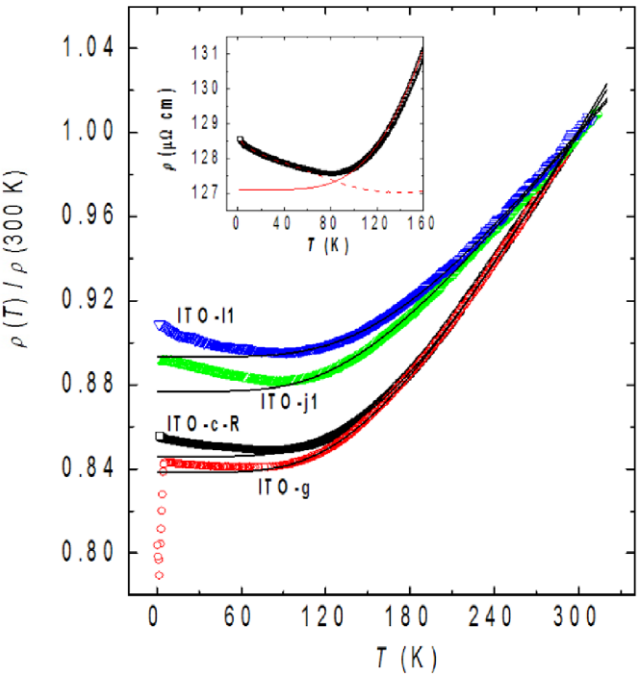

Figure 5. Normalized resistivity, $\rho(T)/\rho(300\,\mathrm{K})$, as a function of temperature for four single-crystalline ITO nanowires with diameters ranging from 110 to 220 nm. The symbols are the experimental data and the solid curves are the theoretical predictions of equation (1). At low temperatures, disorder effects cause resistivity rises with reducing temperature. The ITO-g nanowire reveals a possible superconducting transition. The inset shows the measured resistivity as described by the sum of the Bloch–Grüneisen law (solid curve) and a disorder-induced correction to the residual resistivity ρ_0 (dashed curve) for the ITO-c-R nanowire. This figure was reproduced with permission from [69].

In addition to films and nanowires, nanoscale ITO particles can be made metallic. Ederth *et al* [105] studied the temperature behaviour of porous thin films comprising of ITO nanoparticles. Their films were produced by spin coating a dispersion of ITO nanoparticles (mean grain size ≈16 nm) onto glass substrates, followed by post thermal treatment. They found that the temperature coefficient of resistivity was negative (i.e. $(1/\rho)(d\rho/dT) < 0$) between 77 and 300 K. However, their $\rho(T)$ data obeyed the 'thermally fluctuation-induced-tunnelling conduction' (FITC) process [106–108]. Figure 6 shows the normalized resistivity, $\rho(T)/\rho(273\,\mathrm{K})$, as a function of temperature for four ITO nanoparticle films studied by Ederth *et al*. The symbols are the experimental data and the solid curves are the FITC theory predictions. Theoretically, the FITC model considered the global electrical conduction of an inhomogeneous system consisting of *metal grains* separated by very thin insulating barriers. The thin insulating barriers were modelled as mesoscopic tunnel junctions. Hence, an observation of the FITC processes occurring in porous ITO films implies that the constituent ITO nanoparticles are metallic. Indeed, in section 4, we will discuss that the metallic feature of ITO nanoparticles has provided a powerful platform to experimentally test the recent theories of granular metals [52–57, 109].

We notice in passing that the overall temperature behaviour of resistivity in other TCOs, such as Al-doped

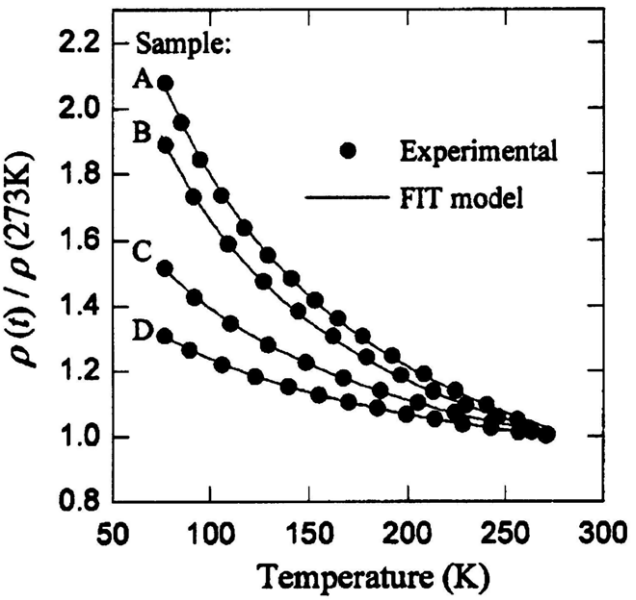

Figure 6. Normalized resistivity, $\rho(T)/\rho(273\,\mathrm{K})$, as a function of temperature for four ITO nanoparticle films. The nanoparticles have a mean grain size ≈16 nm and the films have an approximate thickness ∼1.1 μm. The symbols are the experimental data and the solid curves are the theoretical predictions of the thermally fluctuation-induced-tunnelling conduction process. This figure was reproduced with permission from [105]. Copyright 2003 by the American Physical Society.

ZnO [110–112], Ga-doped ZnO [113, 114], Nb-doped TiO_2 [115, 116] and F-doped SnO_2 [117, 118], can also be described by the standard Boltzmann transport equation (1).

2.3. Linear temperature dependence of thermoelectric power

The thermoelectric power is an important physical quantity which describes the electronic conduction behaviours in the presence of a temperature gradient and under the open circuit situation. Studies of the temperature dependence of thermopower, $S(T)$, can provide useful information about the electronic density of states at the Fermi level $N(E_F)$, the magnitude of E_F, the responsible carrier types (electrons and/or holes), as well as the phonon-electron and phonon-phonon relaxation processes in the material. In a metal, the thermopower arises from two contributions and can be expressed as $S(T) = S_d(T) + S_g(T)$, where $S_d(T)$ is the electron-diffusion contribution and $S_g(T)$ is the phonon-drag contribution [119, 120].

2.3.1. Electron-diffusion thermopower. The electron-diffusion contribution stems from the diffusion of thermal electrons in the presence of a temperature gradient. A general form is given by the Mott formula [119]

$$S_d(T) = -\frac{\pi^2 k_B^2 T}{3|e|E_F}\frac{d\ln\sigma(E)}{d\ln E}\bigg|_{E=E_F}, \qquad (2)$$

where k_B is the Boltzmann constant and $\sigma(E)$ is the conductivity of electrons that have energy E. The Mott formula is derived under the assumption that the phonon distribution is itself in overall equilibrium at temperature T. Note that in the case of hole conduction the minus sign in equation (4) should be replaced by a plus sign.

Consider a free electron Fermi gas. By substituting the Einstein relation $\sigma(E) = N(E)e^2D(E)$ into equation (2), where $D(E) = v^2(E)\tau(E)/3$ is the electron diffusion constant in a 3D conductor with respect to the Boltzmann transport and $v(E)$ is the electron velocity, one obtains

$$S_d(T) = -\frac{\pi^2 k_B^2 T}{3|e|E_F}\left[\frac{3}{2} + \frac{d\ln\tau(E)}{d\ln E}\right]\bigg|_{E=E_F}. \qquad (3)$$

Equation (3) predicts a linear temperature dependence of S_d. The slope of this linear T dependence varies inversely with E_F and its precise value is governed by the energy dependence of mean-free time $\tau(E) \propto E^q$, where q is an exponent of order unity.

The temperature behaviour of S_d in the low temperature limit (which is pertinent to ITO) can be approximated as follows. At $T \ll \theta_D$ and in the presence of notable defect scattering such that the electron mean free path $l(E) = v(E)\tau(E)$ is nearly a constant, i.e. $\tau(E) \propto 1/v(E) \propto 1/\sqrt{E}$, equation (3) reduces to

$$S_d = -\frac{\pi^2 k_B^2 T}{3|e|E_F}. \qquad (4)$$

Since the typical E_F value in ITO is one order of magnitude smaller than that in a typical metal, the S_d value in the former is thus approximately one order of magnitude larger than that in the latter. Alternatively, equation (4) can be rewritten in the following form: $S_d = -2C_e/(3n|e|)$, where $C_e = \pi^2 n k_B^2 T/(2E_F)$ is the electronic specific heat per unit volume. This expression will be used in equation (5).

The temperature behaviour of thermopower in ITO films has been studied by several groups [99, 103, 121, 122]. Figure 7 shows the measured $S(T)$ data between 5 and 300 K for one as-grown and three annealed ITO films. This figure clearly indicates that S is negative and varies essentially *linearly* with T in the *wide* temperature range 5–300 K. The negative sign confirms that electrons are the major charge carriers in ITO.

Recall the fact that the Debye temperature $\theta_D \sim 1000$ K in ITO [69, 99, 104]. Therefore, one may safely ascribe the measured S below 300 K (figure 7) mainly to the diffusion thermopower $S_d(T)$. The straight solid lines in figure 7 are least-squares fits to equation (4). From the extracted slopes, one can compute the E_F value in each sample. The value of electron concentration n can thus be deduced through the free-electron-model expression $E_F = (\hbar^2/2m^*)(3\pi^2 n)^{2/3}$. In ITO structures, the extracted values of E_F generally lie in the range ≈0.5–1 eV [70, 99, 121], corresponding to values of $n \approx 10^{20}$–10^{21} cm^{-3}. Therefore, ITO can be treated as a highly degenerate semiconductor or a low-n metal, as mentioned.

It is worth noting that the n values in ITO films obtained from $S(T)$ measurements agree well with those obtained from the Hall coefficient, $R_H = 1/(n_H e)$, measurements. Figure 8 shows the extracted values of n (squares) and the

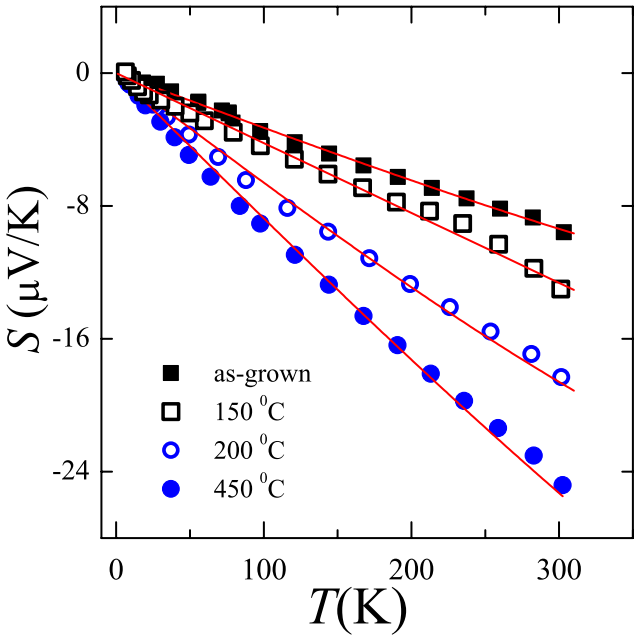

Figure 7. Thermoelectric power as a function of temperature for one as-grown and three O_2 annealed ITO films. The films were 21 nm thick and the thermal annealing was performed at three different temperatures, as indicated. The straight solid lines are least-squares fits to equation (4). This figure was reproduced with permission from [121]. Copyright 2010 by the American Institute of Physics.

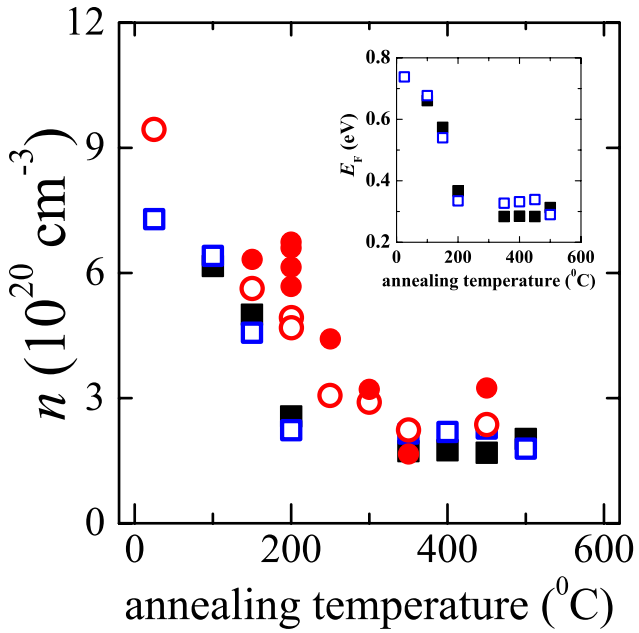

Figure 8. Variation in carrier concentration and Fermi energy with annealing temperature for a good number of 21 nm thick ITO films. Open (closed) squares: n for air (oxygen) annealed films; open (closed) circles: n_H for air (oxygen) annealed films. This figure was reproduced with permission from [121]. Copyright 2010 by the American Institute of Physics.

Hall concentration n_H (circles) for a number of as-grown and annealed ITO films [121]. It is seen that the n values agree with the n_H values to within 30% or better (except for the films annealed at 200 °C, see discussion in [121]). This observation provides a strong experimental support for the validity of the theoretical predictions of a free-carrier-like energy bandstructure in ITO. In fact, such kind of *prevailing linearity* in $S(T)$ from liquid-helium temperatures all the way up to at least 300 K (figure 7) is seldom seen in any textbook simple metals, where the phonon-drag contribution $S_g(T)$ often causes profound, non-monotonic temperature behaviour of $S(T)$ (see, for example, [120] and figures 7.10 and 7.12 in reference [123]). Thus, ITO does serve as a model system for studying electronic conduction phenomena and extracting reliable electronic parameters.

2.3.2. Phonon-drag thermopower. We would like to comment on the negligible phonon-drag contribution to the measured $S(T)$ in the ITO material. The phonon-drag term stems from the interaction between heat conducting phonons with conduction electrons. In ITO (figure 7), the prevailing linearity over a wide range of temperature is a direct and strong indication of the absence of the phonon-drag contribution. The reason for the practically complete suppression of the phonon-drag term can be explained as follows. Considering the phonon scattering processes and ignoring their frequency dependence, the phonon-drag thermopower $S_g(T)$ at $T < \theta_D$ can be approximated by [119, 123]

$$S_g \simeq -\frac{C_g}{3n|e|}\left(\frac{\tau_{\rm ph}}{\tau_{\rm ph}+\tau_{{\rm ph}-e}}\right) \simeq -\frac{C_g}{3n|e|}\left(\frac{\tau_{\rm ph}}{\tau_{{\rm ph}-e}}\right) \simeq \frac{1}{2}\left(\frac{\tau_{\rm ph}}{\tau_{{\rm e}-{\rm ph}}}\right) S_d\,, \qquad (5)$$

where C_g is the lattice specific heat per unit volume, $\tau_{\rm ph}$ is the phonon relaxation time due to all kinds of phonon scattering processes (such as phonon–phonon (ph–ph) scattering, phonon scattering with imperfections, etc) except the phonon–electron (ph–e) scattering and $\tau_{{\rm ph}-e}$ is the ph–e scattering time. In writing equation (5), we have assumed that $\tau_{\rm ph} \ll \tau_{{\rm ph}-e}$. Note that we have also applied the energy-balance equation $C_e/\tau_{{\rm e}-{\rm ph}} = C_g/\tau_{{\rm ph}-e}$ ([124, 125]) to replace $\tau_{{\rm ph}-e}$ by $\tau_{{\rm e}-{\rm ph}}$.

Consider a representative temperature of 100 K $\sim 0.1\theta_D$ in ITO. We take the phonon mean free path to be few nanometres long [126–128], which corresponds to a relaxation time $\tau_{\rm ph}(100\,{\rm K}) \sim 10^{-12}$ s, with a sound velocity $v_p \simeq 4400\,{\rm m\,s^{-1}}$ in ITO [126]. According to our previous studies of the weak-localization effect in ITO films [129], we estimate $\tau_{{\rm e}-{\rm ph}}\,(100\,{\rm K}) \sim 10^{-11}$ s. Thus, equation (5) indicates that the phonon-drag term would contribute only a few percent to the measured thermopower at a temperature of 100 K. The underlying physics for the smallness of the phonon-drag term S_g can further be reasoned as follows. (i) The value of $\tau_{\rm ph}$ in ITO is generally very short due to the presence of a moderately high level of disorder in this class of material. (ii) Since the e–ph coupling strength in a conductor is proportional to the carrier concentration n [101, 129], the relaxation time $\tau_{{\rm e}-{\rm ph}}$ in ITO is thus notably long compared with that in typical metals. (See further discussion in subsection 3.1.2). These two intrinsic material characteristics combine to cause a small $\tau_{\rm ph}/\tau_{{\rm e}-{\rm ph}}$ ratio and hence $S_g \ll S_d$ in the ITO material. By the same token, a linear temperature dependence of $S(T)$ with

negligible contribution from S_g has recently been observed in F-doped SnO_2 films [118].

3. Quantum-interference transport at low temperature: homogeneous indium tin oxide films and nanowires

In section 2, we have examined the temperature dependence of electrical resistivity and thermoelectric power over a wide temperature range to demonstrate that the electronic conduction properties of metallic ITO obey the standard Boltzmann transport equation. In particular, being inherited with a free-carrier-like energy bandstructure, the essential electronic parameters can be reliably extracted from combined $\rho(T)$, $S(T)$ and Hall coefficient R_H measurements. In this section, we show that metallic ITO also opens avenues for the studies of quantum electron transport properties. We shall focus on the quantum-interference weak-localization (WL) effect and the universal conductance fluctuation (UCF) phenomenon, which manifest in ITO films and nanowires at low temperatures. The many-body electron–electron interaction (EEI) effect in homogeneous disordered systems will not be explicitly discussed in this topical review, but will be briefly mentioned where appropriate.

3.1. Weak-localization effect and electron dephasing time

The WL effect and electron dephasing in disordered conductors have been studied for three decades [130–135]. During this time, the mesoscopic and nanoscale physics underlying these processes has witnessed significant theoretical and experimental advances. Over years, the WL effect has also been explored in a few TCO materials, including ITO [67, 129, 136–140] and ZnO based materials [141–143]. In this subsection, we address the experimental 3D, 2D and 1D WL effects in ITO thick films, thin films and nanowires, respectively. In particular, we show that ITO has a relatively long electron dephasing (phase-breaking) length, $L_\varphi(T) = \sqrt{D\tau_\varphi}$ and a relatively weak e–ph relaxation rate $1/\tau_{\text{e–ph}}$, where D is the electron diffusion constant and τ_φ is the electron dephasing time. As a consequence, the WL effect in ITO can persist up to a high measurement temperature of ~100 K. For comparison, in typical normal metals, the WL effect can often be observed only up to ~20–30 K, due to a comparatively strong e–ph relaxation rate as the temperature increases to above liquid-helium temperatures [135]. Furthermore, as a consequence of the small $1/\tau_{\text{e–ph}}$, one may use ITO thick films to explicitly examine the 3D small-energy-transfer electron–electron (e–e) scattering rate, $1/\tau^N_{\text{ee,3D}}$, for the first time in the literature [140]. A long L_φ also causes the 1D WL effect and the UCF phenomenon to significantly manifest in ITO nanowires with diameters $d < L_\varphi$. Since the electronic parameters, such as E_F and D, are well known in ITO, the value of τ_φ can be reliably extracted and closely compared with the theoretical calculations. Such levels of *close comparison* between experimental and theoretical values are nontrivial for many typical metals.

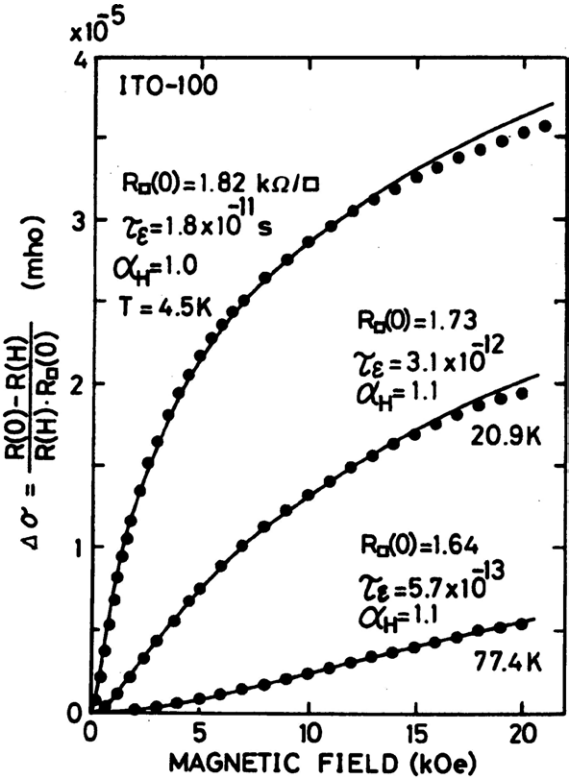

Figure 9. Change in the normalized conductivity with the magnetic field for a 7.5 nm thick ITO film at three temperatures, as indicated. The magnetic field was applied perpendicular to the film plane. The solid curves are the predictions of the 2D WL theory. Note that the quantum-interference WL effect persists up to liquid-nitrogen temperatures in the ITO material. This figure was reproduced with permission from [136]. Copyright 1983 by the Physical Society of Japan.

3.1.1. Weak-localization magnetoresistance in various dimensions. As discussed in section 2, $\rho(T)$ of ITO samples decrease by small amounts ($\lesssim$10% in polycrystalline films and $\lesssim$20% in single-crystalline nanowires) as the temperature decreases from 300 K down to liquid-helium (or liquid-nitrogen) temperatures, suggesting the presence of moderately high levels of disorder in all kinds of ITO materials. Thus, the WL effect must prevail in ITO. In 1983, Ohyama *et al* [136] measured ITO thin films and found negative magnetoresistance (MR) and logarithmic temperature dependence of resistance in a wide temperature range 1.5–100 K. They explained the negative MR in terms of the 2D WL effect and the logarithmic temperature dependence of resistance in terms of a sum of the 2D WL and EEI effects. Figure 9 shows a plot of the positive magnetoconductance (i.e. negative MR) induced by the WL effect in a 7.5 nm thick ITO film measured by Ohyama and coworkers. It is seen that the experimental data (symbols) can be well described by the 2D WL theory predictions (solid curves).

Recently, with the advances of nanoscience and technology, the 1D WL effect has been investigated in single-crystalline ITO nanowires [137–139]. In particular, since L_φ is relatively long in the ITO material at low temperatures (see below), the quasi-1D dimensional criterion $L_\varphi > d$ is readily achieved. Thus, significant 1D WL effects can be seen in

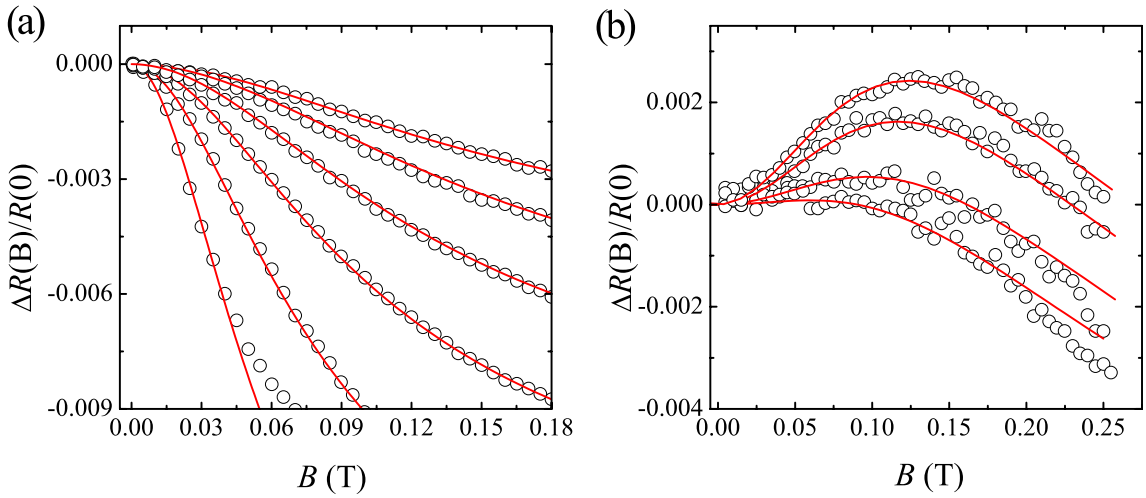

Figure 10. Normalized magnetoresistance, $\Delta R(B)/R(0) = [R(B) - R(0)]/R(0)$, as a function of magnetic field of (*a*) a 60 nm diameter ITO nanowire at (from bottom up): 0.25, 5.0, 12, 20, 30 and 40 K and (*b*) a 72 nm diameter ITO nanowire at (from top down): 0.26, 1.0, 2.0 and 4.0 K. The magnetic field was applied perpendicular to the nanowire axis. The symbols are the experimental data and the solid curves are the 1D WL theory predictions. Note that the MRs are negative in (*a*) (i.e. the weak-localization effect), while positive in (*b*) (i.e. the weak-antilocalization effect) in small magnetic fields. This figure was reproduced with permission from [138]. Copyright 2010 by the American Physical Society.

ITO nanowires. Indeed, figure 10(*a*) shows a plot of the negative MR due to the 1D WL effect in a 60 nm diameter ITO nanowire studied by Hsu *et al* [138]. This nanowire had a low resistivity value of $\rho(10\,\mathrm{K}) \simeq 185\,\mu\Omega\,\mathrm{cm}$. The magnetic field was applied perpendicular to the nanowire axis. The data (symbols) is well described by the 1D WL theory predictions (solid curves). The extracted dephasing lengths are $L_\varphi(0.25\,\mathrm{K}) \simeq 520\,\mathrm{nm}$ and $L_\varphi(40\,\mathrm{K}) \simeq 150\,\mathrm{nm}$. Similarly, the negative MR in the 3D WL effect can be observed in ITO thick films and is well described by the 3D WL theory predictions. (The explicit theoretical predictions for the 1D, 2D and 3D MR in the WL effect can be found in [143] and references therein.)

3.1.2. Electron dephasing time. Measurements of MR in the WL effect allows one to extract the value of τ_φ. Detailed studies of the electron dephasing processes in ITO thin films have recently been carried out by Wu *et al* [129]. They have measured the negative MR due to the 2D WL effect and extracted the τ_φ values in two series of 15 and 21 nm thick ITO films in a wide temperature range 0.3–90 K. Figure 11 shows a plot of representative variation of extracted $1/\tau_\varphi$ with temperature. In general, the responsible dephasing processes are determined by the sample dimensionality, level of disorder and measurement temperature [133, 135, 144]. In 3D weakly disordered metals, e–ph scattering is often the dominant dephasing mechanism [100, 135, 145], while in reduced dimensions (2D and 1D), the e–e scattering is the major dephasing process [135, 144, 146, 147]. As $T \to 0\,\mathrm{K}$, a constant or very weakly temperature dependent dephasing process may exist in a given sample, the physical origin for which is yet to be fully identified [135, 148–152]. In ITO, as already mentioned, the e–ph relaxation rate is very weak.

The total electron dephasing rate $1/\tau_\varphi(T)$ (the solid curves) in figure 11 for the 2D ITO thin films studied by Wu

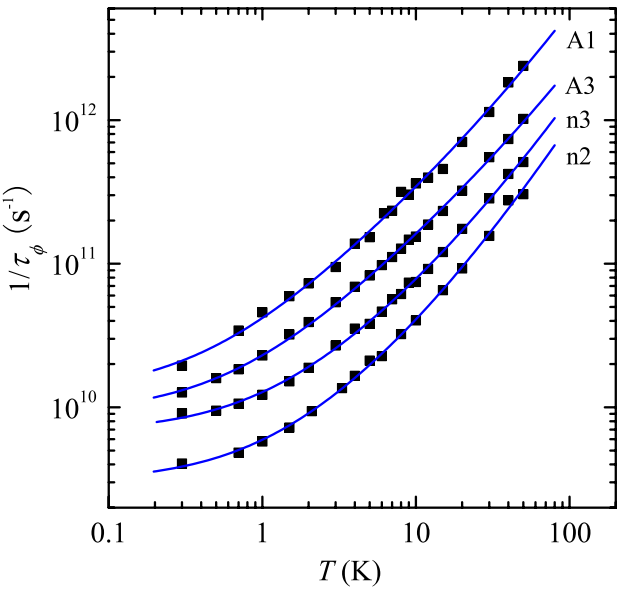

Figure 11. Electron dephasing rate $1/\tau_\varphi$ as a function of temperature for four 15 nm thick ITO films. The solid curves are least-squares fits to equation (6). For clarity, the data for the n3, A3 and A1 films have been shifted up by multiplying by factors of 2, 4 and 8, respectively. This figure was reproduced with permission from [129]. Copyright 2012 by the American Physical Society.

et al [129] is described by

$$\frac{1}{\tau_\varphi(T)} = \frac{1}{\tau_\varphi^0} + A_{\mathrm{ee,2D}}^N T + A_{\mathrm{ee,2D}} T^2 \ln\left(\frac{E_\mathrm{F}}{k_\mathrm{B} T}\right), \qquad (6)$$

where the first, second and third terms on the right-hand side of the equation stand for the 'saturation' term, the small-energy-transfer (Nyquist) e–e scattering term and the large-energy-transfer e–e scattering term, respectively. The small-energy-transfer term is dominant at low temperatures of $T < \hbar/(k_\mathrm{B}\tau_\mathrm{e})$, while the large-energy-transfer term is

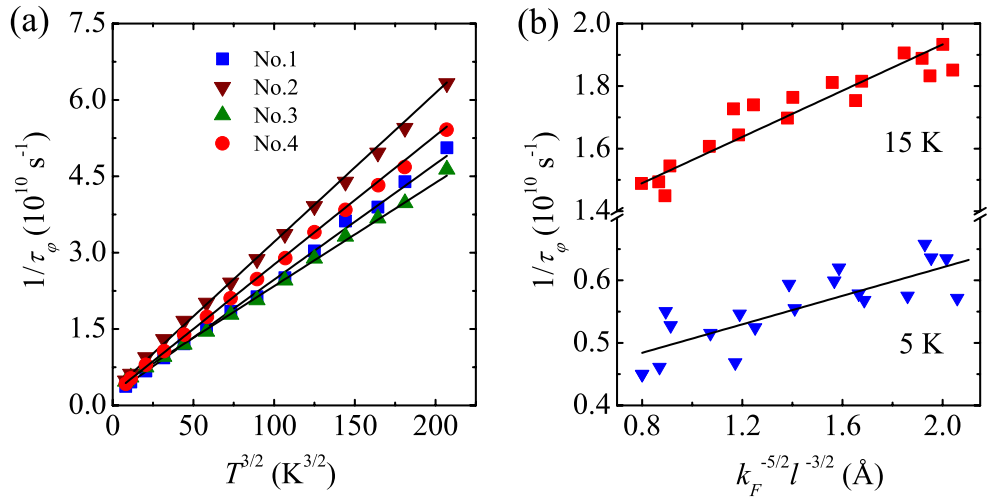

Figure 12. (*a*) Electron dephasing rate $1/\tau_\varphi$ as a function of temperature for four ITO thick films. Note that $1/\tau_\varphi$ varies with a $T^{3/2}$ temperature dependence. (*b*) Variation of $1/\tau_\varphi$ with $k_F^{-5/2} l^{-3/2}$ for a good number of ITO thick films at 5 and 15 K. In the measurement temperature range 4–35 K, the dephasing rate $1/\tau_\varphi \simeq 1/\tau^N_{ee,3D} = A^N_{ee,3D} T^{3/2}$. In (*a*) and (*b*), the solid lines are linear fits. This figure was reproduced with permission from [140].

dominant at high temperatures of $T > \hbar/(k_B \tau_e)$. By comparing their measured $1/\tau_\varphi(T)$ with equation (11), Wu *et al* found that their extracted values of the e–e scattering strengths $A^N_{ee,2D} \approx 3 \times 10^9\,K^{-1}\,s^{-1}$ and $A_{ee,2D} \approx 9 \times 10^6\,K^{-2}\,s^{-1}$ are consistent with the theoretical values to within a factor of ~ 3 and ~ 5, respectively[5]. Considering that the ITO material is a disordered $In_{2-x}Sn_xO_{3-\delta}$ with random Sn dopants and possible oxygen vacancies, such levels of agreement between experimental and theoretical values are satisfactory. The good theoretical estimates must derive from the free-carrier-like energy bandstructure characteristics of ITO, which renders evaluations of the electronic parameters reliable. In terms of dephasing length, figure 11 gives rise to relatively long length scales of $L_\varphi(0.3\,K) \approx 500\,nm$ and $L_\varphi(60\,K) \approx 45\,nm$.

The e–e scattering rate in other-dimensional ITO samples has also been studied. In the case of 1D nanowires, due to the sample dimensionality effect, the Nyquist e–e scattering rate obeys a $1/\tau^N_{ee,1D} \propto T^{2/3}$ temperature law [135, 144]. This scattering process is largely responsible for the 1D WL MR shown in figures 10(*a*) and (*b*), as analyzed and discussed in [138]. In the case of 3D thick films, the temperature dependence of the Nyquist rate changes to the $1/\tau^N_{ee,3D} \propto T^{3/2}$ temperature law [153, 154]. Owing to the intrinsic weak e–ph coupling in this material, ITO provides a valuable platform for detailed study of the 3D small-energy-transfer e–e scattering process over wide ranges of temperature and disorder, as discussed below.

In a 3D weakly disordered metal, the e–e scattering rate has been calculated by Schmid in 1974 and his result is given by [153]

$$\frac{1}{\tau_{ee}} = \frac{\pi}{8}\frac{(k_B T)^2}{\hbar E_F} + \frac{\sqrt{3}}{2\hbar\sqrt{E_F}}\left(\frac{k_B T}{k_F l}\right)^{3/2}. \qquad (7)$$

A similar result has also been obtained by Altshuler and Aronov [154]. The first term on the right-hand side of equation (7) is the e–e scattering rate in a perfect, periodic potential, while the second term is the enhanced contribution due to the presence of imperfections (defects, impurities, interfaces, etc) in the sample. Microscopically, the second term stands for the Nyquist e–e scattering process and is dominant at low temperatures of $T < \hbar/(k_B \tau_e)$, while the first term represents the large-energy-transfer process and dominates at high temperatures of $T > \hbar/(k_B \tau_e)$ ([131, 154]). We shall denote the second term by $1/\tau^N_{ee,3D} = A^N_{ee,3D} T^{3/2}$. In 3D weakly disordered typical metals, the e–ph scattering is strong and dominates over the e–e scattering [135]. Thus, equation (7) has been difficult to test in a quantitative manner for decades, even though the mesoscopic physics has witnessed marvellous advances.

Very recently, Zhang *et al* [140] have measured the low magnetic field MRs in a series of 3D ITO films with thicknesses exceeding 1 micrometre. Their polycrystalline samples were prepared by the standard RF sputtering deposition method in an Ar and O_2 mixture. During deposition, the oxygen content, together with the substrate temperature, was varied to 'tune' the electron concentration as well as the amount of disorder. By comparing the MR data with the 3D WL theory, Zhang *et al* extracted the dephasing rate $1/\tau_\varphi$ as plotted in figure 12(*a*). Clearly, one observes a strict $1/\tau_\varphi \propto T^{3/2}$ temperature dependence in a wide T range 4–35 K. Quantitatively, the scattering rate of the first term in equation (7) is about one order of magnitude smaller than that of the second term even at $T = 35\,K$ in ITO. Thus, the contribution of the first term can be safely ignored. The straight solid lines in figures 12(*a*) are described by $1/\tau_\varphi = 1/\tau^0_\varphi + A^N_{ee,3D} T^{3/2}$, where $1/\tau^0_\varphi$ is

[5] The theoretical expressions for the small-energy-transfer and large-energy-transfer e–e scattering strengths, respectively, are $A^N_{ee,2D} = (e^2/2\pi\hbar^2) R_\square k_B \ln(\pi\hbar/e^2 R_\square)$ and $A_{ee,2D} = \pi k_B^2/(2\hbar E_F)$, where $R_\square$ is the sheet resistance. In the comparison of experiment with theory, the $R_\square$ value was directly measured and the E_F value was extracted from thermoelectric power measurement.

a constant and $A^N_{ee,3D} \simeq (2.1\text{–}2.8)\times10^8\,\mathrm{K}^{-3/2}\,\mathrm{s}^{-1}$ for various samples. These experimental $A^N_{ee,3D}$ values are within a factor of ~3 of the theoretical values given by the second term of equation (7).

Furthermore, applying the free-electron model, Zhang *et al* [140] rewrote the second term on the right hand of equation (7) into the form $1/\tau^N_{ee,3D} = A^N_{ee,3D}T^{3/2} = (1.22\sqrt{m^*}/\hbar^2)(k_BT)^{3/2}k_F^{-5/2}l^{-3/2}$. This expression allows one to check the combined disorder ($k_F^{-3/2}l^{-3/2}$) and carrier concentration (k_F^{-1}) dependence of $1/\tau^N_{ee,3D}$ at a given temperature. Figure 12(*b*) shows a plot of the variation of the extracted $1/\tau_\varphi$ with $k_F^{-5/2}l^{-3/2}$ at two T values of 5 and 15 K. Obviously, a variation $1/\tau_\varphi \propto k_F^{-5/2}l^{-3/2}$ is observed. Quantitatively, the experimental slopes ($\simeq 1.2\times10^{19}$ and $3.7\times10^{19}\,\mathrm{m}^{-1}\,\mathrm{s}^{-1}$ at 5 and 15 K, respectively) in figure 12(*b*) are within a factor of ~5 of the theoretical values. Thus, the experimental dephasing rate $1/\tau_\varphi \simeq 1/\tau^N_{ee,3D} = A^N_{ee,3D}T^{3/2}$ in ITO thick films quantitatively confirms the temperature, disorder and carrier concentration dependences of the Schmid-Altshuler-Aronov theory of 3D small-energy-transfer e–e scattering in disordered metals [153, 154].

Electron–phonon relaxation rate. We would like to comment on the reason why the e–e scattering dominates the electron dephasing rate in 3D ITO thick films (figure 12) in a wide T range up to several tens of degrees of kelvin. The reason is owing to the fact that the ITO material possesses relatively low n values which result in a greatly suppressed $1/\tau_{e\text{–}ph} \ll 1/\tau^N_{ee,3D}$. Theoretically, it is established that the electron scattering by transverse vibrations of defects and impurities dominates the e–ph relaxation. In the quasi-ballistic limit ($q_Tl > 1$, where q_T is the wavenumber of a thermal phonon)[6], the electron-transverse phonon scattering rate is given by [101, 145, 155]

$$\frac{1}{\tau_{e-t,ph}} = \frac{3\pi^2k_B^2\beta_t}{(p_Fu_t)(p_Fl)}T^2, \tag{8}$$

where $\beta_t = (2E_F/3)^2N(E_F)/(2\rho_mu_t^2)$ is the electron-transverse phonon coupling constant, p_F is the Fermi momentum, u_t is the transverse sound velocity and ρ_m is the mass density. Since the electronic parameters E_F, p_F, $N(E_F)$ and l in ITO samples are known, the theoretical value of equation (8) can be computed and is of the magnitude $1/\tau_{e-t,ph} \sim 4\times10^6\,T^2\,\mathrm{K}^{-2}\,\mathrm{s}^{-1}$. Note that this relaxation rate is about one order of magnitude smaller than $1/\tau^N_{ee,3D}$ even at a relatively high temperature of 40 K. A weak e–ph relaxation rate allows the quantum-interference WL effect and UCF phenomena to persist up to a few tens of degrees of kelvin in ITO[7].

[6] In high-quality ITO structures, $q_Tl \approx 0.1\,T$ [129, 140] and hence the quasi-ballistic limit is valid above ~10 K. In disordered normal metals, due to a relatively short electron mean free path $l = 3\pi^2\hbar/(e^2k_F^2\rho) \propto 1/k_F^2$ for a same ρ value, the quasi-ballistic regime is more difficult to realize in experiment. For example, a polycrystalline $Ti_{73}Al_{27}$ alloy [38] (an amorphous CuZrAl alloy [157]) with $\rho \approx 225\,\mu\Omega\,\mathrm{cm}$ ($\approx 200\,\mu\Omega\,\mathrm{cm}$) has a value of $q_Tl \approx 0.006\,T$ (≈0.01 T).

[7] The electron dephasing length $L_\varphi = \sqrt{D\tau_\varphi} \simeq \sqrt{D\tau_{e\text{–}ph}}$ above a few degrees of kelvin is much shorter in a typical disordered metal than in ITO, due to both a much shorter $\tau_{e\text{–}ph}$ and a smaller diffusion constant $D \propto 1/(N(E_F)\rho) \propto 1/N(E_F)$ for a same ρ value in the former.

We reiterate that equation (8) predicts a relaxation rate $1/\tau_{e-t,ph} \propto n$. On the other hand, equation (7) predicts a scattering rate $1/\tau^N_{ee,3D} \propto n^{-5/6}$. Thus, the ratio of these two scattering rates varies approximately inversely with the square of n, namely, $(1/\tau^N_{ee,3D})/(1/\tau_{e-t,ph}) \propto n^{-2}$. Since the n values in ITO samples are relatively low, the 3D small-energy-transfer e–e scattering rate can thus be enhanced over the e–ph relaxation rate. This observation can be extended to other TCO materials and is worth of further investigations.

We also would like to note that, in recent studies of superconducting hot electron bolometers, a *weak* e–ph relaxation rate has been observed in quasi-2D heterostructures containing ultrathin $La_{2-x}Sr_xCuO_4$ (LSCO) layers [156]. LSCO has a n value about two orders of magnitude lower that in the conventional superconductor NbN and hence $\tau_{e\text{–}ph}$(LSCO) is nearly two orders of magnitude longer than $\tau_{e\text{–}ph}$(NbN). In short, we remark that slow e–ph relaxation is a general intrinsic property of low-n conductors. Generally speaking, one may keep in mind that the relaxation rate varies approximately as $1/\tau_{e\text{–}ph} \propto n$ ([155, 156]).

Spin–orbit scattering time. According to the recent measurements on a good number of ITO films [129] and nanowires [138] down to as low as 0.25 K, only *negative* MR was observed (see, for example, figure 10(*a*)). This result suggests that the spin–orbit scattering rate, $1/\tau_{so}$, is relatively weak in ITO. Even at sub-kelvin temperatures where the inelastic electron scattering events are scarce, one still obtains $1/\tau_{so} < 1/\tau^N_{ee}(0.25\,\mathrm{K})$ in many ITO samples. In other words, the ITO material possesses an inherent long spin–orbit scattering length $L_{so} = \sqrt{D\tau_{so}}$. In typical ITO films [129], the extracted length scale is $L_{so} > 500\,\mathrm{nm}$, corresponding to a scattering time $\tau_{so} > 250\,\mathrm{ps}$. This τ_{so} value is one to two orders of magnitude longer than those in typical metals, such as Ag films [158] and Sn-doped $Ti_{73}Al_{27}$ alloys [38].

In practice, the strength of spin–orbit coupling in a given metal can be tuned by varying the level of disorder. In general, the spin–orbit scattering rate can be approximately expressed by $1/\tau_{so} \propto Z^4/\tau_e \propto \rho$, where Z is the atomic number of the relevant (heavy) scatterer. Indeed, an enhancement of the spin–orbit scattering rate has been achieved in an ITO nanowire which was intentionally made to have a high resistivity value of $\rho(10\,\mathrm{K}) = 1030\,\mu\Omega\,\mathrm{cm}$ [138]. Hsu *et al* then observed positive MR at temperatures $T < 4\,\mathrm{K}$ in low magnetic fields, see figure 10(*b*). A positive MR is a direct manifestation of the weak-antilocalization effect which results from the scattering rates $1/\tau_{so} > 1/\tau^N_{ee,1D}$ at $T < 4\,\mathrm{K}$. At higher temperatures, a negative MR was recovered, suggesting that $1/\tau_{so} < 1/\tau^N_{ee,1D}$ at $T > 4\,\mathrm{K}$. In this high-ρ ITO nanowire, Hsu *et al* obtained a moderate length scale $L_{so} \approx 95\,\mathrm{nm}$, corresponding to a scattering time $\tau_{so} \approx 15\,\mathrm{ps}$. The capability of tuning the spin–orbit coupling strength might be useful for the future implementation of nanoscale spintronic devices [159]. Recently, Shinozaki *et al* [160] have observed an increasing ratio $(1/\tau_{so})/(1/\tau^N_{ee,3D})$ with increasing ρ in a series of amorphous indium-zinc-oxide and indium-(tin,gallium)-zinc-oxide thick films.

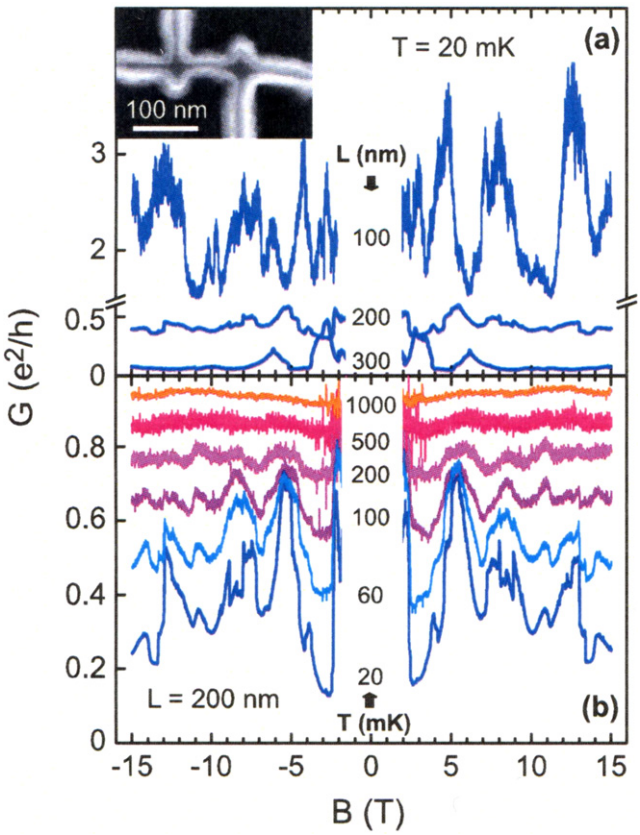

Figure 13. (*a*) Universal conductance fluctuations for three ∼20 nm wide (Ga, Mn)As wires with different lengths $L \simeq 100$, 200 and 300 nm. The inset shows an electron micrograph of the 100 nm long wire. (*b*) Conductance G versus magnetic field B for the 200 nm long wire at several temperatures below 1 K. The magnetic field was applied perpendicular to the wire axis. This figure was reproduced with permission from [168]. Copyright 2006 by the American Physical Society.

3.2. Universal conductance fluctuations

Universal conductance fluctuations (UCFs) are a fundamental phenomenon in mesoscopic physics. The UCFs originate from the quantum interference between electron partial waves that propagate along different trajectories in a miniature system in which *classical self-averaging* is absent or incomplete [161–164]. Thus, the shape of the UCF patterns (called 'magneto-fingerprints') is very sensitive to the specific *impurity configuration* of a given sample. The UCFs have previously been experimentally observed in lithographic metal and semiconductor mesoscopic structures at low temperatures [163, 165, 166], where the electron dephasing length L_φ is comparable to the sample size. Recently, UCFs have been observed in new artificial materials, including epitaxial InAs nanowires [167], lithographic ferromagnets [168], carbon nanotubes [169], graphene [170] and topological insulators [171, 172]. These new observations in artificially synthesized materials have enriched and deepened quantum electron transport physics.

Wagner *et al* [168] have measured the UCFs in lithographically defined ferromagnetic (Ga, Mn)As nanowires. Figure 13(*a*) shows their measured conductance G as a function of magnetic field B for three wires at $T = 20$ mK. The wires were ∼20 nm wide and 100, 200, or 300 nm long. Figure 13(*b*) shows G versus B at several different temperatures between 20 mK and 1 K for the 200 nm long wire. The magnetic field was applied perpendicular to the wire axis. Figure 13(*b*) clearly reveals that the UCFs are observable below ∼0.5 K. Figure 13(*a*) demonstrates that the UCF amplitude decreases with increasing sample length, suggesting a fairly short dephasing length of $L_\varphi(20\,\text{mK}) \approx 100$ nm. For the 100 nm long wire, the peak-to-peak UCF amplitude reaches a value of e^2/h at 20 mK, where h is the Planck constant.

Impurity reconfiguration. Let us return to the case of ITO. Since L_φ can reach ≈500 nm at low temperatures, the ITO nanowires are very useful for the investigations of the 1D UCF phenomena. Yang *et al* [139] have recently carried out the magneto-transport measurements on individual ITO nanowires with a focus on studying the UCFs. Their nanowires were made by implanting Sn ions into $In_2O_{3-\delta}$ nanowires. Figures 14(*a*)–(*d*) show four plots of the variation of the UCFs, denoted by $\delta G_{\text{UCF}}(T, B)$, with magnetic field B for a 110 nm diameter ITO nanowire at several temperatures[8]. The magnetic field was applied perpendicular to the nanowire axis. Here, after the first run at liquid-helium temperatures, the nanowire was thermally cycled to room temperature, at which it stayed overnight and cooled down again for the magneto-transport measurements at liquid-helium temperatures. The thermal cycling to room temperature was repeated twice and the sample was thus measured for three times at three different cooldowns. The idea was that a thermal cycling to 300 K could possibly induce *impurity reconfiguration* in the given nanowire. A new impurity configuration must lead to differing trajectories of the propagating electron partial waves, which in turn cause distinct quantum interference. As a result, the shape of the UCF patterns should be completely changed. Figure 14(*a*) shows $\delta G_{\text{UCF}}(T, B)$ as a function of B at several temperatures measured at the first cooldown. Figure 14(*b*) shows $\delta G_{\text{UCF}}(T, B)$ as a function of B at several temperatures measured at the second cooldown and figure 14(*c*) shows those measured at the third cooldown.

A number of important UCF features and the underlying physics can be learned from close inspection of these figures.

(i) Inspection of figures 14(*a*)–(*c*) indicates that the UCF magnitudes decrease with increasing temperature and disappear at ∼25 K. Thus, these quantum conductance fluctuations are distinctly different from the classical thermal noise whose resistance fluctuation magnitudes increase with increasing temperature.

(ii) During a given cooldown, the shape of the UCF patterns at different temperatures remains the same to a large extent. This observation implies that the impurity configuration is frozen for a considerable period of time if the nanowire is constantly kept at liquid-helium temperatures. A given impurity configuration gives rise to a specific 'magneto-fingerprint', strongly suggesting that the UCF phenomena is a robust manifestation of an intrinsic quantum-interference effect.

[8] The universal conductance fluctuation $\delta G_{\text{UCF}}(T, B)$ is defined by subtracting a smooth magneto-conductance background (including the WL MR contribution) from the measured $G(T, B)$.

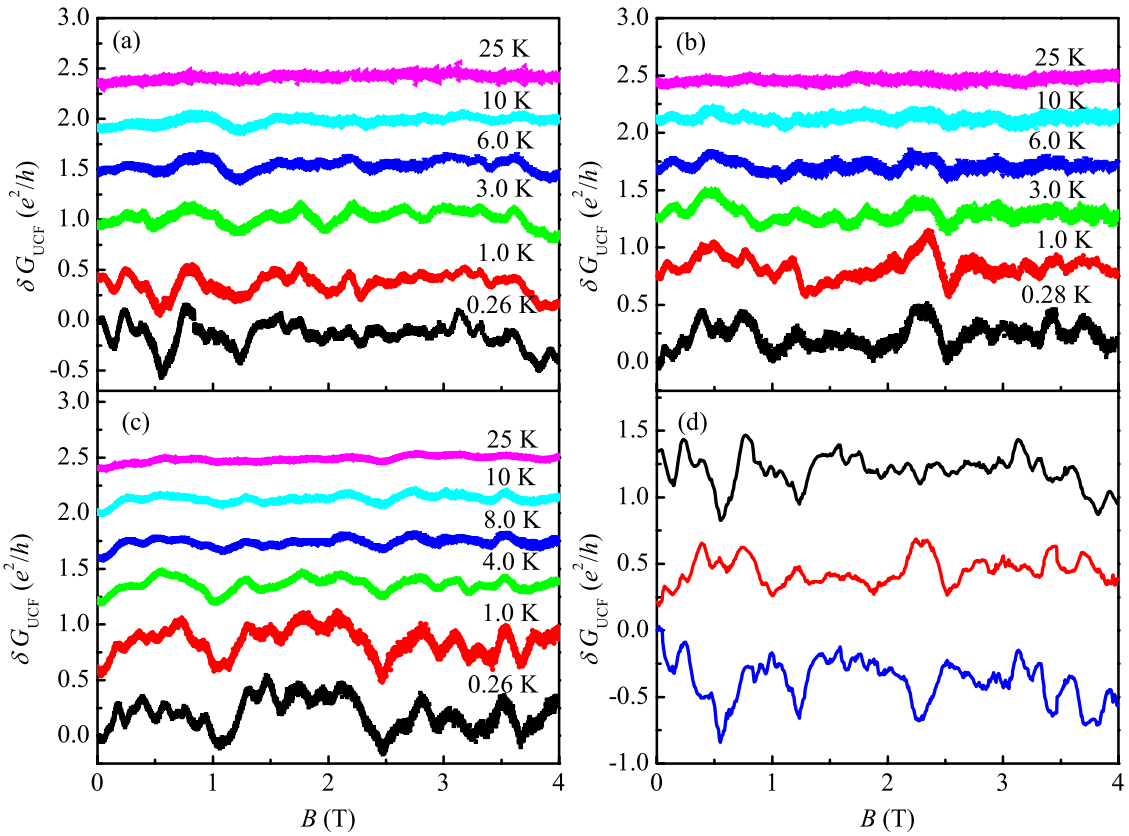

Figure 14. Variation of the UCFs, $\delta G_{\rm UCF}(T, B)$, with magnetic field at several temperatures for a 110 nm diameter and 1.2 μm long ITO nanowire at (*a*) first cooldown, (*b*) second cooldown and (*c*) third cooldown. (*d*) The $\delta G_{\rm UCF}(T = 0.26\,{\rm K})$ curves taken from panel (*a*) (top curve) and panel (*b*) (middle curve) and their difference (bottom curve), as a function of magnetic field. The magnetic field was applied perpendicular to the nanowire axis. In panels (*a*)–(*d*), the UCF curves are vertically offset for clarity. This figure was reproduced with permission from [139]. Copyright 2012 by the American Physical Society.

(iii) At a given temperature, the UCFs among different cooldowns reveal similar peak-to-peak magnitudes.

(iv) Figure 14(*d*) shows a plot of the $\delta G_{\rm UCF}(T = 0.26\,{\rm K}, B)$ curves taken from figure 14(*a*) (top curve) and figure 14(*b*) (middle curve) and their difference (bottom curve). This figure is convenient for close inspection and comparison. The top two curves reveal completely different shapes of the UCF patterns, strongly reflecting that a thermal cycling to 300 K has induced an impurity reconfiguration. On the other hand, the UCF magnitudes of these two curves retain similar, with a peak-to-peak value of $\delta G_{\rm UCF}(T = 0.26\,{\rm K}) \approx 0.5\, e^2/h$ for both curves. The reason for retaining a similar UCF magnitude is as follows. The UCF magnitudes in a given nanowire are governed by the L_φ values, which are determined by the level of disorder, i.e. the ρ value (or the $R_\square$ value in 2D), see section 3.1.2. The ρ ($R_\square$) value of a sample is determined by the total number of impurities, but insensitive to the specific spatial distribution of the impurities (provided that the impurity concentration is uniform throughout the sample)[9].

[9] The UCF studies also allow extractions of the $L_\varphi(T)$ values in a miniature sample. The values thus obtained are in fair accord with those extracted from the WL MR measurements. In addition to L_φ, the thermal diffusion length L_T plays a key role in governing the UCF magnitudes.

Classical self-averaging and thermal averaging at finite temperatures. In the case of a quasi-1D wire with length L, the UCF theory predicts a root-mean-square conductance fluctuation magnitude of $\sqrt{\langle(\delta G_{\rm UCF})^2\rangle} \simeq 0.73\, e^2/h$ in the limit of $T \to 0\,{\rm K}$ [161, 162, 164]. At this low T limit, the wire behaves as a single phase-coherent regime. As the temperature gradually increases from absolute zero, $L_\varphi(T)$ becomes progressively shorter and one has to take into account the classical self-averaging effect. That is, the phase-coherent regime is expected to be cut off by L_φ and the UCF magnitude $\sqrt{\langle(\delta G_{\rm UCF})^2\rangle}$ is predicted to be suppressed by a factor $(L_\varphi/L)^{3/2}$ under the condition $L_\varphi < L_T$, where $L_T = \sqrt{D\hbar/k_{\rm B}T} \propto 1/\sqrt{T}$ is the thermal diffusion length defined in the EEI theory. The suppression of the UCF magnitudes originates from the fact that the UCFs of different phase-coherent regimes fluctuate statistically independently. If the temperature further increases such that $L_T < L_\varphi$ or, equivalently, the thermal energy exceeds the Thouless energy $k_{\rm B}T > \hbar/\tau_\varphi$, one also has to take into account the *thermal averaging* effect. That is, the phase-coherent regime is now expected to be cut off by L_T and the UCF magnitude $\sqrt{\langle(\delta G_{\rm UCF})^2\rangle}$ is predicted to be suppressed by a factor $(L_T/L)\sqrt{L_\varphi/L}$. These theoretical concepts have been well accepted by the mesoscopic physics communities for three decades, but have rarely been experimentally tested in

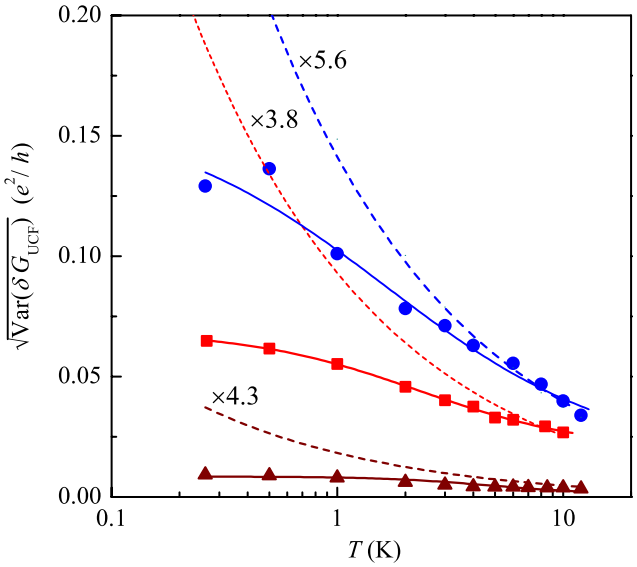

Figure 15. Variation of measured $\sqrt{\langle(\delta G_{\rm UCF})^2\rangle}$ (denoted by the square root of the variance $\sqrt{{\rm Var}(\delta G_{\rm UCF})}$ in ordinate) magnitudes with temperature for three ITO nanowires with diameter and length: circles (110 nm and 1.2 μm), squares (78 nm and 1.4 μm) and triangles (72 nm, 2.8 μm). The solid curves drawn through the data points are guides to the eye. The dashed curves are the UCF theory predictions by taking into account both the classical self-averaging and the thermal averaging effects. The thermal averaging effect due to L_T varies approximately as $1/\sqrt{T}$, while the self-averaging effect due to L_φ possesses a very weak temperature dependence. The theoretical and experimental values are normalized for 10 K in each nanowire. Note that the theoretical predictions diverge significantly from the experimental results. This figure was reproduced with permission from [139]. Copyright 2012 by the American Physical Society.

a quantitative manner. The lack of experimental information was mainly due to the fact that the UCFs could be observed only at temperatures below 1 K in conventional lithographic metal and semiconductor mesoscopic structures. Fortunately, the observations of the UCFs in ITO nanowires over a wide range of temperature from below 1 K up to above 10 K now provides us with a unique opportunity to verify these subtle UCF theory predictions.

Figure 15 shows a plot of the variation of measured $\sqrt{\langle(\delta G_{\rm UCF})^2\rangle}$ with temperature for three ITO nanowires studied by Yang *et al* [139]. Surprisingly, the theoretical predictions invoking the thermal averaging effect (dashed curves) diverge significantly from the measured UCF magnitudes (symbols). In figure 15, the theoretical curves vary approximately as $1/\sqrt{T}$, while the experiment reveals a much slower temperature dependence. In other words, the phase-coherent regime in the 1D UCF phenomenon is not cut off by L_T, even though the experiment well satisfied the condition $k_{\rm B}T > \hbar/\tau_\varphi$ ($L_T < L_\varphi$). The reason why the thermal averaging effect played no significant role in figure 15 is not understood. The ITO nanowires make experimentally feasible to re-examine whether any ingredients in the theoretical concepts for thermal averaging in mesoscopic physics might have been overlooked (overestimated).

In summary, the UCF phenomena manifest rich and subtle quantum-interference properties of a mesoscopic or nanoscale structure. They provide crucial information about the impurity configuration in a particular sample. In ITO nanowires, the UCF signals persist up to 20–30 K. For comparison, recall that in conventional lithographic metal samples, the UCFs (including magnetic-field dependent UCFs and temporal UCFs [173]) can only be observed at sub-kelvin temperatures [168]. Such pronounced conductance fluctuations provide valuable opportunities for critical examinations of the underlying UCF physics [139, 174]. The presence of marked UCFs suggest that there must exist a large amount of point defects in artificially synthesized ITO nanostructures, even though the nanowires exhibit a single crystalline structure under high-resolution transmission electron microscopy studies[10].

4. Many-body electron transport in granular metals: inhomogeneous indium tin oxide ultrathin films

In this section, we discuss the electrical-transport properties of *inhomogeneous* ITO ultrathin films (average thickness $\approx$ 5–15 nm) which reveal new many-body physical phenomena that are absent in *homogeneous* disordered systems. These new physical properties, including logarithmic temperature dependences of both longitudinal electrical conductivity and Hall transport in a wide range of temperature, have recently been theoretically predicted [52–57], but not yet experimentally tested in detail.

Generally speaking, granular metals are composite materials that are composed of finely dispersed mixtures of immiscible metal and insulator grains. In many cases, the insulating constituent may form an amorphous matrix [176, 177]. In terms of electrical-transport properties, three distinct regimes can be achieved in a given granular system, i.e. the metallic, the insulating (dielectric) and the metal-insulator transition regimes. These three regimes can be conveniently categorized by a quantity called G_T. Here G_T is the average tunnelling conductance between neighbouring (metal) grains and is a key parameter which determines the global electrical properties of a given granular array. G_T can be expressed in units of $e^2/\hbar$ and written as $G_T = g_T(2e^2/\hbar)$, where $\hbar$ is the Planck constant divided by 2π and g_T is a dimensionless average tunnelling conductance. The factor 2 arises from the two allowed spin directions for a tunnelling electron. When $g_T > g_T^c$ ($g_T < g_T^c$) the system lies in the metallic (insulating) regime. A metal-insulator transition occurs at $g_T = g_T^c$. Here $g_T^c = (1/2\pi\tilde{d})\ln(E_{\rm c}/\tilde{\delta})$ is a critical dimensionless tunnelling conductance whose value depends on the dimensionality of the granular array $\tilde{d}$, where $E_{\rm c}$ is the charging energy and $\tilde{\delta}$ is the mean energy level spacing in a grain (references [52, 55]). In experiments, the magnitude of g_T^c is of order unity or somewhat smaller [109, 178].

Over decades, there has been extensive theoretical and experimental research on the microstructures and electrical-transport properties of granular systems [177]. New discoveries have continuously been made and a good understanding of the physical properties conceptualized. For

[10] We note that it has recently been found that high levels of point defects appear in most artificially grown single-crystalline nanostructures, including ITO, RuO_2 [174] and ZnO [175] nanowires.

example, the giant Hall effect (GHE) has recently been discovered in $Cu_v(SiO_2)_{1-v}$ [179] and $Mo_v(SnO_2)_{1-v}$ [180] granular films under the conditions that the grain size $a \ll L_\varphi$ and the metal volume fraction v is around the quantum percolation threshold v_q [181]. The GHE is a novel physical phenomenon which manifests a huge Hall coefficient R_H that is enhanced by ~3 orders of magnitude when v approaches v_q from the metallic side. The GHE is theoretically explained to arise from the local quantum-interference effect in the presence of rich microstructures in a metal-insulator composite constituting of nanoscale granules [181]. While the single-particle local quantum interference causes the new GHE, in the following discussion we shall focus on the many-body electronic transport properties in granular systems.

In the rest of this section, we concentrate on the region with $g_T \gg 1$ or $g_T \gg g_T^c$. The material systems that we are interested in can thus be termed 'granular metals'. In particular, we shall demonstrate that inhomogeneous ITO ultrathin films are an ideal granular metal system which provides valuable and unique playgrounds for critically testing the recent theories of granular metals. These new theories of granular metals are concerned with the many-body electron–electron (e–e) interaction effect in inhomogeneous disordered systems. They focus on the electronic conduction properties in the temperature regime above moderately low temperatures ($T > g_T\tilde{\delta}/k_B$) where the WL effect is predicted to be comparatively small or negligible [52, 182]. In practice, one can explicitly measure the e–e interaction effect by applying a weak perpendicular magnetic field to suppress the quantum-interference WL effect.

4.1. Longitudinal electrical conductivity

For a long time, the electrical-transport properties of granular metals have not been explicitly considered theoretically. It has widely been taken for granted that the transport properties would be similar to those in homogeneous disordered metals [131]. It was only recently that Efetov, Beloborodov and coworkers have investigated the many-body Coulomb e–e interaction effect in granular metals. They [52–55] found that the influences of e–e interaction on the longitudinal electrical conductivity $\sigma(T)$ and the electronic density of states $N(E)$ in granular metals are dramatically different from those in homogeneous disordered metals. In particular, for granular metals with $g_0 \gg g_T$ and $g_T \gg 1$, the *intergrain* e–e interaction effect causes a correction to σ in the temperature range $g_T\tilde{\delta} < k_BT < E_c$. Here $g_0 = G_0/(2e^2/\hbar)$ and G_0 is the conductance of a single metal grain. In this temperature interval of practical experimental interest, the total conductivity is given by [53–55]

$$\sigma = \sigma_0 + \delta\sigma = \sigma_0\left[1 - \frac{1}{2\pi g_T \tilde{d}}\ln\left(\frac{g_T E_c}{k_B T}\right)\right], \quad (9)$$

where $\sigma_0 = G_T a^{2-\tilde{d}}$ is the tunnelling conductivity between neighbouring grains in the absence of Coulomb interaction and a is the average radius of the metal grain. Note that the correction term $\delta\sigma$ is negative and possesses a logarithmic temperature dependence. That is, the Coulomb e–e interaction slightly suppresses intergrain electron tunnelling conduction, giving rise to $\delta\sigma/\sigma_0 \propto -1/g_T$ for $g_T \gg 1$. This $\delta\sigma \propto \ln T$ temperature law is robust and independent of the array dimensionality $\tilde{d}$. It should also be noted that this correction term $\delta\sigma$ does not exist in the EEI theory of homogeneous disordered metals [131].

Soon after the theoretical prediction of equation (9), the electrical-transport properties of several granular systems were studied, including Pt/C composite nanowires [183, 184], B-doped nano-crystalline diamond films [185] and granular Cr films [178]. The $\delta\sigma \propto \ln T$ temperature law has been confirmed. In addition, a large suppression in the electronic density of states around the Fermi energy $N(E_F)$ has been found in studies of the differential conductances of $Al/AlO_x/Cr$ tunnel junctions [178] and thin Pd-ZrO_2 granular films [186]. This last experimental result also qualitatively confirmed the prediction of the theory of granular metals [52, 187]. However, a quantitative comparison is not possible, due to the lack of a theoretical expression for $N(T, V)$ at finite voltages and finite temperatures.

Figure 16 shows the variation of longitudinal electrical conductivity with logarithm of temperature for four inhomogeneous ITO ultrathin films studied by Zhang *et al* [109]. These films were grown by the RF deposition method onto glass substrates. They were ≈10 ± 3 nm thick and the average grain sizes were in the range ≈24–38 nm. Therefore, the samples can be treated as 2D random granular arrays. (Each sample was nominally covered by one layer of ITO granules.) The conductivities were measured in a perpendicular magnetic field of 7 T in order to suppress any residual 2D WL effect. Inspection of figure 16 clearly demonstrates a $\delta\sigma \propto \ln T$ variation over a wide temperature range from ~3 K to T^*, where $T^* = T^*(E_c)$ is the maximum temperature below which the $\ln T$ law holds. Therefore, the prediction of equation (9) is confirmed. Quantitatively, from the least-squares fits (the straight solid lines in figure 16), values of the intergrain tunnelling conductance $g_T \simeq 7$–31 were obtained. Therefore, the theoretical criterion of $g_T \gg 1$ for equation (9) to be valid is satisfied. We reiterate that the $\delta\sigma \propto \ln T$ temperature law observed in figure 16 is not due to the more familiar 2D EEI effect which widely appears in homogeneous disordered systems [109].

4.2. Hall transport

Apart from the longitudinal electrical conductivity, Kharitonov and Efetov [56, 57] have investigated the influence of Coulomb interaction on the Hall resistivity, ρ_{xy}, by taking the electron dynamics *inside* individual grains into account. They found that there also exists a correction to the Hall resistivity in the wide temperature range $g_T\tilde{\delta} \lesssim k_BT \lesssim \min(g_T E_c, E_{Th})$, where $E_{Th} = D_0\hbar/a^2$ is the Thouless energy of a grain of radius a, D_0 is the electron diffusion constant in the grain and $\min(g_T E_c, E_{Th})$ denotes the minimum value of the set

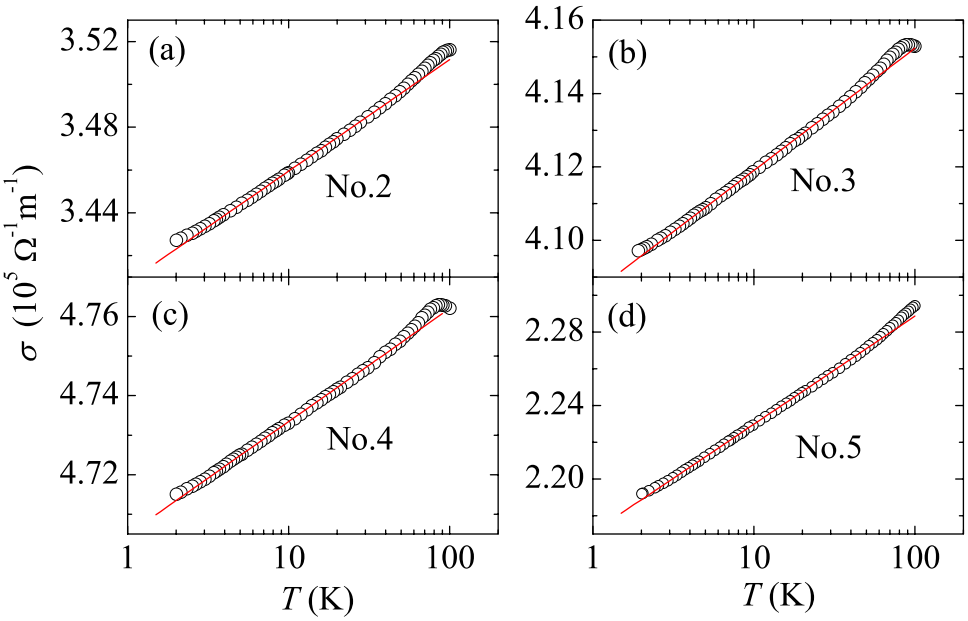

Figure 16. Variation of longitudinal electrical conductivity with logarithm of temperature for four inhomogeneous ITO ultrathin films measured in a perpendicular magnetic field of 7 T. The average film thickness (in nm), average grain size (in nm) and fitted g_T value in each film are (*a*) 9.2, 28 and 13 (*b*) 11, 34 and 23 (*c*) 13, 38 and 31 and (*d*) 7.6, 24 and 7.4, respectively. The solid straight lines are least-squares fits to equation (9). This figure was reproduced with permission from [109]. Copyright 2011 by the American Physical Society.

$(g_T E_c,\ E_{Th})$. The resulting Hall resistivity is given by [56, 57]

$$\rho_{xy}(T) = \rho_{xy,0} + \delta\rho_{xy} = \frac{B}{n^* e}\left[1 + \frac{c_d}{4\pi g_T}\ln\left(\frac{\min(g_T E_c,\ E_{Th})}{k_B T}\right)\right], \quad (10)$$

where n^* is the effective carrier concentration, c_d is a numerical factor of order unity and $\rho_{xy,0} = B/(n^* e)$ is the Hall resistivity of the granular array in the absence of the Coulomb e–e interaction effect. We point out that the microscopic mechanisms leading to the $\ln T$ temperature behaviours in equations (9) and (10) are distinctly different. The longitudinal conductivity correction $\delta\sigma$ originates from the renormalization of intergrain tunnelling conductance g_T, while the Hall resistivity correction $\delta\rho_{xy}$ stems from virtual electron diffusion inside individual grains [56, 57].

As mentioned previously, the theoretical predication of equation (9) has been experimentally tested in a few granular systems. On the contrary, the prediction of equation (10) is far more difficult to verify in real material systems. The major reason is due to the fact that the $\rho_{xy,0}$ magnitude ($\propto 1/n^*$) in a granular metal with $g_T \gg 1$ is already small and difficult to measure. Obviously, the e–e interaction induced correction term $\delta\rho_{xy}$ is even much smaller. Typically, the ratio $\delta\rho_{xy}/\rho_{xy,0} \sim 1/g_T$ is on the order of a few percent and equation (10) is a perturbation theory prediction.

In section 2, we have stressed that the carrier concentration in the ITO material is ~ 2 to 3 orders of magnitude lower than those in typical metals. Thus, generally speaking, the Hall coefficient, $R_H = \rho_{xy}/B$, in ITO granular films would be ~ 2 to 3 orders of magnitude larger than those in conventional granular films made of normal-metal granules. Hence, the theoretical predication of equation (10) can be experimentally tested by utilizing inhomogeneous ITO ultrathin films.

In addition to the observation in figure 16, Zhang *et al* [109] have studied the Hall transport in inhomogeneous ITO ultrathin films. Figure 17 shows the temperature dependence of R_H for four samples they have measured. Evidently, one sees a robust $R_H \propto \ln T$ variation over a wide temperature range from ~ 2 K to T_{max}, where T_{max} is a temperature below which the $\ln T$ law holds. The T_{max} value for a given granular array is determined by the constituent grain parameters E_c and E_{Th} as well as the intergrain tunnelling parameter g_T. For those ITO ultrathin films shown in figure 17, the experimental T_{max} values varied from $\sim$50 to $\sim$120 K. Quantitatively, the correction term contributes a small magnitude of $[R_H(2\,\mathrm{K}) - R_H(T_{max})]/R_H(T_{max}) \simeq \delta\rho_{xy}(2\,\mathrm{K})/\rho_{xy,0} \lesssim 5\%$, where $R_H(T_{max}) \simeq 1/(n^* e)$ is the Hall coefficient in the absence of the Coulomb e–e interaction effect. The experimental data (symbols) can be well described by the theoretical predictions (solid straight lines) with satisfactory values of the adjustable parameters. Thus, the prediction of equation (10) is experimentally confirmed for the first time in the literature.

In summary, the simultaneous experimental observations of $\delta\sigma \propto \ln T$ (figure 16) and $\delta\rho_{xy} \propto \ln T$ (figure 17) laws over a wide range of temperature from liquid-helium temperature up to and above liquid-nitrogen temperature strongly support the recent theoretical concepts for charge transport in granular metals, i.e. equations (9) and (10), which are formulated under the condition that the intergrain tunnelling conductivity $g_T \gg 1$. We note again that the free-carrier-like and, especially, the low-n characteristics of the ITO material have made possible a close experimental examination of equation (10). While measurements of $\delta\sigma$ are relatively easy, finding a proper granular metal with $g_T \gg 1$ to measure the small correction term $\delta\rho_{xy}$ is definitely nontrivial. The ITO material made into

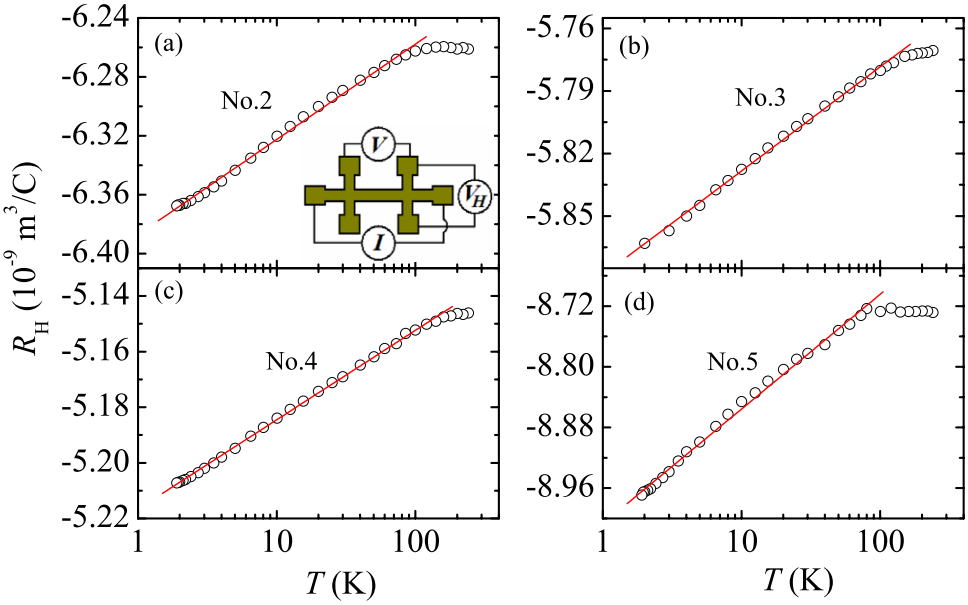

Figure 17. Hall coefficient as a function of logarithm of temperature for four inhomogeneous ITO ultrathin films. These films are the same as those shown in figure 16. The solid straight lines are least-squares fits to equation (10). The inset in (*a*) depicts a schematic for the Hall-bar-shaped sample. This figure was reproduced with permission from [109]. Copyright 2011 by the American Physical Society.

an inhomogeneous ultrathin film form has opened up avenues for exploring the many-body Coulomb effects in condensed matter physics.

Recently, the thermoelectric power in the presence of granularity and in the limit of $g_T \gg 1$ has been theoretically calculated [188]. It was predicted that the granularity could lead to substantial improvement in thermodynamic properties and, in particular, the figure of merit of granular materials could be high. Experimental investigations in this direction would be worthwhile in light of the development of useful thermoelectric materials. On the other hand, it has recently been reported that the presence of granularity causes an enhancement of the flicker noise ($1/f$ noise) level in ITO films. This is ascribed to atomic diffusion along grain boundaries or dynamics of two-level systems near the grain boundaries [189]. Since the $1/f$ noise could potentially hinder the miniature device performance, it would be of interest and importance to explore its properties in inhomogeneous ITO ultrathin films.

5. Conclusion

Indium tin oxide (ITO) is a very interesting and useful transparent conducting oxide (TCO) material. It is stable at ambient conditions and can be readily grown into a variety of forms, including polycrystalline thin and thick films and single-crystalline nanowires. Simultaneously, they can have electrical resistivities as low as $\approx 150\,\mu\Omega\,$cm at room temperature and optical transparencies as high as $\approx$90% transmittance at the visible light frequencies. Apart from their technological issues, the electronic conduction properties of ITO have rarely been systematically explored as a condensed matter physics research subject and down to fundamental levels. In this topical review, we have focused on metallic ITO structures. We have shown that the overall electrical resistivity and thermoelectric power can be described by the Boltzmann transport equation. A linear dependence on temperature of thermoelectric power in a wide range of temperature eloquently manifests the free-carrier-like energy bandstructure around the Fermi level of this class of material. At liquid-helium temperatures, marked weak-localization effect and universal conductance fluctuations emerge. ITO provides a rich playground for studying these quantum interference phenomena in all three dimensions, which leads to an improved understanding of the underlying physics governing the properties of mesoscopic and nanoscale structures. Inhomogeneous ITO ultrathin films have opened up unique and valuable avenues for studying the many-body electron–electron interaction effect in granular metals. These new theoretical predictions cannot be addressed by employing conventional granular systems.

The objective of this topical review is not only to present the charge transport properties of ITO but also to demonstrate that the ITO material is versatile and powerful for unravelling new physics. Microscopically, the intrinsic electronic properties that make ITO an appealing technological as well as academic material are the free-carrier-like energy bandstructure and a low level of carrier concentration. Owing to the inherent free-carrier-like characteristics, the electronic parameters can be reliably evaluated through the free-electron model, which in turn facilitate critical tests of a variety of lasting and new theoretical predictions. A low carrier concentration gives rise to slow electron–phonon relaxation, which manifests the linear electron diffusion thermoelectric power and also yields a weak electron dephasing rate in the ITO material. In light of the development and search for useful TCOs, it would be of great interest to investigate whether the numerous aspects of the novel electronic conduction properties that we have addressed in this topical review might also manifest in other, such as ZnO- and SnO_2-based, TCO materials.

Acknowledgments

The authors thank Y Galperin, A Sergeev and I Beloborodov for valuable suggestions and comments and D Rees for careful reading of the manuscript. We are grateful to S-P Chiu, Y-F Chen, C-Y Wu, Y-W Hsu, B-T Lin, P-Y Yang and Y-J Zhang for their collaborations at the various stages of our lasting research on ITO. JJL also would like to thank H-F Meng for incidentally igniting his interest in the marvellous electronic conduction properties of the ITO material a decade ago. This work was supported at NCTU by the Taiwan Ministry of Science and Technology through Grant No. NSC 102-2120-M-009-003 and the MOE ATU Program, and at TJU by the NSF of China through Grant No. 11174216 and the Research Fund for the Doctoral Program of Higher Education through Grant No. 20120032110065.

References

[1] Holland L 1956 *Vacuum Deposition of Thin Films* (New York: Wiley) p 492
[2] Jarzębski Z M 1982 *Phys. Status Solidi* **71** 13
[3] Facchetti A and Marks T J 2010 *Transparent Electronics: from Synthesis to Applications* (Chichester: Wiley)
[4] Ginley D S and Bright C 2000 *MRS Bull.* **25** 15
[5] Granqvist C G and Hultåker A 2002 *Thin Solid Films* **411** 1
[6] Granqvis C G 2007 *Sol. Energy Mater. Sol. Cells* **91** 1529
[7] Hamberg I, Granqvist C G, Berggren K F, Sernelius B E and Engström L 1984 *Phys. Rev.* B **30** 3240
[8] Gerfin T and Grätzel M 1996 *J. Appl. Phys.* **79** 1722
[9] Schröer P, Krüger P and Pollmann J 1993 *Phys. Rev.* B **47** 6971
[10] Imai Y J, Watanabe A and Shimono I 2003 *J. Mater. Sci.: Mater. Electron.* **14** 149
[11] Imai Y J and Watanabe A 2004 *J. Mater. Sci.: Mater. Electron.* **15** 743
[12] Karazhanov S Z, Ravindran P, Kjekshus A, Fjellvåg H and Svensson B G 2007 *Phys. Rev.* B **75** 155104
[13] Kılıç Ç and Zunger A 2002 *Phys. Rev. Lett.* **88** 095501
[14] Robertson J 1984 *Phys. Rev.* B **30** 3520
[15] Mishra K C, Johnson K H and Schmidt P C 1995 *Phys. Rev.* B **51** 13972
[16] Li Z Q, Yin Y L, Liu X D and Song Q G 2009 *J. Appl. Phys.* **106** 083701
[17] Schleife A, Varley J B, Fuchs F, Rödl C, Bechstedt F, Rinke P, Janotti A and Van de Walle C G 2011 *Phys. Rev.* B **83** 035116
[18] Liu X D, Jiang E Y, Li Z Q and Song Q G 2008 *Appl. Phys. Lett.* **92** 252104
[19] Osorio-Guillén J, Lany S and Zunger A 2008 *Phys. Rev. Lett.* **100** 036601
[20] Orita N 2010 *Japan. J. Appl. Phys.* **49** 055801
[21] Chen D M, Xu G, Miao L, Chen L H, Nakao S and Jin P 2010 *J. Appl. Phys.* **107** 063707
[22] Huy H A, Aradi B, Frauenheim T and Deák P 2011 *Phys. Rev.* B **83** 155201
[23] Yamamoto T and Ohno T 2012 *Phys. Rev.* B **85** 033104
[24] Yang Y, Jin S, Medevdeva J E, Ireland J R, Metz A W, Ni J, Hersam M C, Freeman A J and Marks T J 2005 *J. Am. Chem. Soc.* **127** 8796
[25] Medevdeva J E and Freeman A J 2005 *Europhys. Lett.* **69** 583
[26] Odaka H, Shigesato Y, Murakami T and Iwata S 2001 *Japan. J. Appl. Phys.* **40** 3231
[27] Mryasov O N and Freeman A J 2001 *Phys. Rev.* B **64** 233111
[28] Medvedeva J E 2006 *Phys. Rev. Lett.* **97** 086401
[29] Medvedeva J E and Hettiarachchi C L 2010 *Phys. Rev.* B **81** 125116
[30] King P D C, Veal T D, Payne D J, Bourlange A, Egdell R G and McConville C F 2008 *Phys. Rev. Lett.* **101** 116808
[31] King P D C, Veal T D, McConville C F, Zúñiga Pérez J, Muñoz Sanjosé V, Hopkinson M, Rienks E D L, Jensen M F and Hofmann P 2010 *Phys. Rev. Lett.* **104** 256803
[32] Lany S, Zakutayev A, Mason T O, Wager J F, Poeppelmeier K R, Perkins J D, Berry J J, Ginley D S and Zunger A 2012 *Phys. Rev. Lett.* **108** 016802
[33] Zhang K H L, Egdell R G, Offi F, Iacobucci S, Petaccia L, Gorovikov S and King P D C 2013 *Phys. Rev. Lett.* **110** 056803
[34] Taga N, Shigesato Y and Kamei M 2000 *J. Vac. Sci. Technol.* A **18** 1663
[35] Rauf I A 1996 *J. Appl. Phys.* **79** 4057
[36] Kittel C 2005 *Introduction to Solid State Physics* 8th edn (New York: Wiley)
[37] Lin J J, Yu C and Yao Y D 1993 *Phys. Rev.* B **48** 4864
[38] Hsu S Y, Sheng P J and Lin J J 1999 *Phys. Rev.* B **60** 3940
[39] Guillén C and Herrero J 2007 *J. Appl. Phys.* **101** 073514
[40] Kim H, Gilmore C M, Piqué A, Horwitz J S, Mattoussi H, Murata H, Kafafi Z H and Chrisey D B 1999 *J. Appl. Phys.* **86** 6451
[41] Chopra K L, Major S and Pandya D K 1983 *Thin Solid Films* **102** 1
[42] Hamberg I and Granqvist C G 1986 *J. Appl. Phys.* **60** R123
[43] Lewis B G and Paine D C 2000 *MRS Bull.* **25** 22
[44] Kawazoe K, Yanagi H, Ueda K and Hosono H 2000 *MRS Bull.* **25** 28
[45] Minami T 2000 *MRS Bull.* **25** 38
[46] Freeman A J, Poeppelmeier K R, Mason T O, Chang R P H and Marks T J 2000 *MRS Bull.* **25** 45
[47] Gordon R G 2000 *MRS Bull.* **25** 52
[48] Coutts T J, Young D L and Li X 2000 *MRS Bull.* **25** 58
[49] Exarhos G J and Zhou X D 2007 *Thin Solid Films* **515** 7025
[50] Hosono H 2007 *Thin Solid Films* **515** 6000
[51] King P D C and Veal T D 2011 *J. Phys.: Condens. Matter* **23** 334214
[52] Beloborodov I S, Lopatin A V, Vinokur V M and Efetov K B 2007 *Rev. Mod. Phys.* **79** 469
[53] Efetov K B and Tschersich A 2003 *Phys. Rev.* B **67** 174205
[54] Efetov K B and Tschersich A 2002 *Europhys. Lett.* **59** 114
[55] Beloborodov I S, Efetov K B, Lopatin A V and Vinokur V M 2003 *Phys. Rev. Lett.* **91** 246801
[56] Kharitonov M Yu and Efetov K B 2007 *Phys. Rev. Lett.* **99** 056803
[57] Kharitonov M Yu and Efetov K B 2008 *Phys. Rev.* B **77** 045116
[58] Liu C, Matsutani T, Asanuma T, Murai M, Kiuchi M, Alves E and Reis M 2003 *J. Appl. Phys.* **93** 2262
[59] Iwatsubo S 2006 *Vacuum* **80** 708
[60] Shigesato Y, Koshi-ishi R, Kawashima T and Ohsako J 2000 *Vacuum* **59** 614
[61] Liu X D, Jiang E Y and Zhang D X 2008 *J. Appl. Phys.* **104** 073711
[62] Kytin V G, Kulbachinskii V A, Reukova O V, Galperin Y M, Johansen T H, Diplas S and Ulyashin A G 2014 *Appl. Phys. A: Mater. Sci. Process.* **114** 957
[63] Mott N F and Davis E A 1979 *Electronic Processes in Non-Crystalline Materials* 2nd edn (Clarendon: Oxford)
[64] Shklovskii B I and Efros A L 1984 *Electronic Properties of Doped Semiconductors* (Berlin: Springer)
[65] Sheng P, Abeles B and Arie Y 1973 *Phys. Rev. Lett.* **31** 44
[66] Beloborodov I S, Lopatin A V and Vinokur V M 2005 *Phys. Rev.* B **72** 125121
[67] Ohyama T, Okamoto M and Otsuka E 1985 *J. Phys. Soc. Japan* **54** 1041
[68] Mori N 1993 *J. Appl. Phys.* **73** 1327
[69] Chiu S P, Chung H F, Lin Y H, Kai J J, Chen F R and Lin J J 2009 *Nanotechnology* **20** 105203

[70] Aliev A E, Xiong K, Cho K and Salamon M B 2012 *Appl. Phys. Lett.* **101** 252603
[71] Fan J C C and Goodenough J B 1977 *J. Appl. Phys.* **48** 3524
[72] Fuchs F and Bechstedt F 2008 *Phys. Rev.* B **77** 155107
[73] Kikuchi N, Kusano E, Nanto H, Kinbara A and Hosono H 2000 *Vacuum* **59** 492
[74] Huang K F, Uen T M, Gou Y S, Huang C R and Yan H C 1987 *Thin Solid Films* **148** 7
[75] Shigesato Y, Paine D C and Haynes T E 1993 *J. Appl. Phys.* **73** 3805
[76] Taga N, Odaka H, Shigesato Y, Yasui I, Kamei M and Haynes T E 1996 *J. Appl. Phys.* **80** 978
[77] Mizuhashi M 1980 *Thin Solid Films* **70** 91
[78] Agnihotry S A, Saini K K, Saxena T K, Nagpal K C and Chandra S 1985 *J. Phys.* D **18** 2087
[79] Jan S W and Lee S C 1987 *J. Electrochem. Soc.* **134** 2056
[80] Nanto H, Minami T, Orito S and Takata S 1988 *J. Appl. Phys.* **63** 2711
[81] Wu W F and Chiou B S 1994 *Thin Solid Films* **247** 201
[82] Joshi R N, Singh V P and McClure J C 1995 *Thin Solid Films* **257** 32
[83] Wu C Y, Lin B T, Zhang Y J and Lin J J 2012 *Phys. Rev.* B **85** 104204
[84] Kane J and Schweizer H P 1975 *Thin Solid Films* **29** 155
[85] Ryabova L A, Salun V S and Serbinov I A 1982 *Thin Solid Films* **92** 327
[86] Maruyama T and Fukui K 1991 *Thin Solid Films* **203** 197
[87] Xu J J, Shaikh A S and Vest R W 1988 *Thin Solid Films* **161** 273
[88] Furusaki T and Kodaira K 1991 *High Performance Ceramic Films and Coatings* ed P Vincenzini (Amsterdam: Elsevier) p 241
[89] Nishio K, Sei T and Tsushiya T 1996 *J. Mater. Sci.* **31** 1761
[90] Alam M J and Cameron D C 2000 *Thin Solid Films* **377–378** 455
[91] Ramaiah K S, Raja V S, Bhatnagar A K, Tomlinson R D, Pilkington R D, Hill A E, Chang S J, Su Y K and Juang F S 2000 *Semicond. Sci. Technol.* **15** 676
[92] Hichoua A E, Kachouaneb A, Bubendorffc J L, Addoub M, Ebothec J, Troyonc M and Bougrine A 2004 *Thin Solid Films* **458** 263
[93] Moholkar A V, Pawar S M, Rajpure K Y, Ganesan V and Bhosale C H 2008 *J. Alloys Compounds* **464** 387
[94] Guo E J, Guo H, Lu H, Jin K, He M and Yang G 2011 *Appl. Phys. Lett.* **98** 011905
[95] Bierwagen O and Speck J S 2014 *Phys. Status Solidi* a **211** 48
[96] Ohta H, Orita M, Hirano M, Tanji H, Kawazoe H and Hosono H 2000 *Appl. Phys. Letts.* **76** 2740
[97] Nistor M, Perriére J, Hebert C and Seiler W 2010 *J. Phys.: Condens. Matter* **22** 045006
[98] Seiler W, Nistor M, Hebert C and Perrière J 2013 *Sol. Energy Mater. Sol. Cells* **116** 34
[99] Li Z Q and Lin J J 2004 *J. Appl. Phys.* **96** 5918
[100] Zhong Y L and Lin J J 1998 *Phys. Rev. Lett.* **80** 588
[101] Zhong Y L, Sergeev A, Chen C D and Lin J J 2010 *Phys. Rev. Lett.* **104** 206803
[102] Wu C Y, Jian W B and Lin J J 1998 *Phys. Rev.* B **57** 11232
[103] Lin B T, Chen Y F, Lin J J and Wu C Y 2010 *Thin Solid Films* **518** 6997
[104] Preissler N, Bierwagen O, Ramu A T and Speck J S 2013 *Phys. Rev.* B **88** 085305
[105] Ederth J, Johnsson P, Niklasson G A, Hoel A, Hultåker A, Heszler P, Granqvist C G, van Doorn A R and Jongerius M J 2003 *Phys. Rev.* B **68** 155410
[106] Sheng P, Sichel E K and Gittleman J I 1978 *Phys. Rev. Lett.* **40** 1197
[107] Sheng P 1980 *Phys. Rev.* B **21** 2180
[108] Lin Y H, Chiu S P and Lin J J 2008 *Nanotechnology* **19** 365201
[109] Zhang Y J, Li Z Q and Lin J J 2011 *Phys. Rev.* B **84** 052202
[110] Bamiduro O, Mustafa H, Mundle R, Konda R B and Pradhan A K 2007 *Appl. Phys. Lett.* **90** 252108
[111] Liu X D, Liu J, Chen S and Li Z Q 2012 *Appl. Surf. Sci.* **263** 486
[112] Yang Y, Zhang Y J, Liu X D and Li Z Q 2012 *Appl. Phys. Lett.* **100** 262101
[113] Bhosle V, Tiwari A and Narayan J 2006 *Appl. Phys. Lett.* **88** 032106
[114] Ahn B D, Oh S H, Kim H J, Jung M H and Ko Y G 2007 *Appl. Phys. Lett.* **91** 252109
[115] Furubayashi Y, Hitosugi T, Yamamoto Y, Inaba K, Kinoda G, Hirose Y, Shimada T and Hasegawa T 2005 *Appl. Phys. Lett.* **86** 252101
[116] Zheng X W and Li Z Q 2009 *Appl. Surf. Sci.* **255** 8104
[117] Amorim C A, Dalmaschio C J, Melzi A L R, Leite E R and Chiquito A J 2014 *J. Phys. Chem. Solids* **75** 583
[118] Lang W J and Li Z Q 2014 *Appl. Phys. Lett.* accepted (arXiv:1406.5269)
[119] MacDonald D K C 1962 *Thermoelectricity: an Introduction to the Principles* (New York: Wiley)
[120] Siebold T and Ziemann P 1995 *Phys. Rev.* B **51** 6328
[121] Wu C Y, Thanh T V, Chen Y F, Lee J K and Lin J J 2010 *J. Appl. Phys.* **108** 123708
[122] Guilmeau E, Bérardan D, Simon C, Maignan A, Raveau B, Ovono D O and Delorme F 2009 *J. Appl. Phys.* **106** 053715
[123] Blatt F J 1970 *Physics of Electronic Conduction in Solids* (New York: McGraw-Hill)
[124] Reizer M Yu and Sergeev A V 1986 *Sov. Phys.—JETP* **63** 616
[125] Sergeev A V and Reizer M Yu 1996 *Int. J. Mod. Phys.* B **10** 635
[126] Ashida T, Miyamura A, Oka N, Sato Y, Yagi T, Taketoshi N, Baba T and Shigesato Y 2009 *J. Appl. Phys.* **105** 073709
[127] Cordfunke E H P and Westrum E F Jr 1992 *J. Phys. Chem. Solids* **53** 361
[128] Wang L M, Chang C Y, Yeh S T, Chen S W, Peng Z A, Bair S C, Lee D S, Liao F C and Kuo Y K 2012 *Ceram. Int.* **38** 1167
[129] Wu C Y, Lin B T, Zhang Y J, Li Z Q and Lin J J 2012 *Phys. Rev.* B **85** 104204
[130] Bergmann G 1984 *Phys. Rep.* **107** 1
[131] Altshuler B L and Aronov A G 1985 *Electron–Electron Interactions in Disordered Systems* ed A L Efros and M Pollak (Amsterdam: Elsevier)
[132] Fukuyama H 1985 *Electron–Electron Interactions in Disordered Systems* ed A L Efros and M Pollak (Amsterdam: Elsevier)
[133] Lee P A and Ramakrishnan T V 1985 *Rev. Mod. Phys.* **57** 287
[134] Chakravarty S and Schmid A 1986 *Phys. Rep.* **140** 193
[135] Lin J J and Bird J P 2002 *J. Phys.: Condens. Matter* **14** R501
[136] Ohyama T, Okamoto M and Otsuka E 1983 *J. Phys. Soc. Japan* **52** 3571
[137] Chiquito A J, Lanfredi A J C, de Oliveira R F M, Pozzi L P and Leite E R 2007 *Nano Lett.* **7** 1439
[138] Hsu Y W, Chiu S P, Lien A S and Lin J J 2010 *Phys. Rev.* B **82** 195429
[139] Yang P Y, Wang L Y, Hsu Y W and Lin J J 2012 *Phys. Rev.* B **85** 085423
[140] Zhang Y J, Li Z Q and Lin J J 2013 *Europhys. Lett.* **103** 47002
[141] Liu X D, Jiang E Y and Li Z Q 2007 *J. Appl. Phys.* **102** 073708
[142] Shinozaka B, Makise K, Shimane Y, Nakamura H and Inoue K 2007 *J. Phys. Soc. Japan* **76** 074718
[143] Chiu S P, Lu J G and Lin J J 2013 *Nanotechnology* **24** 245203
[144] Altshuler B L, Aronov A G and Khmelnitsky D E 1982 *J. Phys.* C **15** 7367
[145] Rammer J and Schmid A 1986 *Phys. Rev.* B **34** 1352
[146] Fukuyama H and Abrahams E 1983 *Phys. Rev.* B **27** 5976

[147] Pierre F, Gougam A B, Anthore A, Pothier H, Esteve D and Birge N O 2003 *Phys. Rev.* B **68** 085413
[148] Lin J J and Giordano N 1987 *Phys. Rev.* B **35** 1071
[149] Huang S M, Lee T C, Akimoto H, Kono K and Lin J J 2007 *Phys. Rev. Lett.* **99** 046601
[150] Lin J J, Li T J and Zhong Y L 2003 *J. Phys. Soc. Japan* **72** 7
[151] Golubev D S and Zaikin A D 2007 *Physica* E **40** 32
[152] Rotter I 2009 *J. Phys.* A **42** 153001
[153] Schmid A 1974 *Z. Phys.* **271** 251
[154] Altshuler B L and Aronov A G 1979 *JETP Lett.* **30** 482
[155] Sergeev A and Mitin V 2000 *Phys. Rev.* B **61** 6041
[156] Wen B, Yakobov R, Vitkalov S A and Sergeev A 2013 *Appl. Phys. Lett.* **103** 222601
[157] Li L, Lin S T, Dong C and Lin J J 2006 *Phys. Rev.* B **74** 172201
[158] Bergmann G and Horriar-Esser C 1985 *Phys. Rev.* B **31** 1161
[159] Žutić I, Fabian J and Sarma S D 2004 *Rev. Mod. Phys.* **76** 323
[160] Shinozaki B, Hidaka K, Ezaki S, Makise K, Asano T, Tomai S, Yano K and Nakamura H 2013 *J. Appl. Phys.* **113** 153707
[161] Lee P A and Stone A D 1985 *Phys. Rev. Lett.* **55** 1622
[162] Lee P A, Stone A D and Fukuyama H 1987 *Phys. Rev.* B **35** 1039
[163] Washburn S and Webb R A 1986 *Adv. Phys.* **35** 375
[164] Beenakker C W J and van Houten H 1988 *Phys. Rev.* B **37** 6544
[165] Washburn S and Webb R A 1992 *Rep. Prog. Phys.* **55** 1311
[166] Thornton T J, Pepper M, Ahmed H, Davies G J and Andrews D 1987 *Phys. Rev.* B **36** 4514
[167] Hansen A E, Björk M T, Fasth C, Thelander C and Samuelson L 2005 *Phys. Rev.* B **71** 205328
[168] Wagner K, Neumaier D, Reinwald M, Wegscheider W and Weiss D 2006 *Phys. Rev. Lett.* **97** 056803
[169] Man H T and Morpurgo A F 2005 *Phys. Rev. Lett.* **95** 026801
[170] Berezovsky J, Borunda M F, Heller E J and Westervelt R M 2010 *Nanotechnology* **21** 274013
[171] Checkelsky J G, Hor Y S, Cava R J and Ong N P 2011 *Phys. Rev. Lett.* **106** 196801
[172] Chiu S P and Lin J J 2013 *Phys. Rev.* B **87** 035122
[173] Beutler D E, Meisenheimer T L and Giordano N 1987 *Phys. Rev. Lett.* **58** 1240
[174] Lien A S, Wang L Y, Chu C S and Lin J J 2011 *Phys. Rev.* B **84** 155432
[175] Chiu S P, Lin Y H and Lin J J 2009 *Nanotechnology* **20** 015203
[176] Abeles B, Sheng P, Coutts M D and Arie Y 1975 *Adv. Phys.* **24** 407
[177] Abeles B 1976 *Applied Solid State Science: Advance in Materials and Device Research* ed R Wolf (New York: Academic)
[178] Sun Y C, Yeh S S and Lin J J 2010 *Phys. Rev.* B **82** 054203
[179] Zhang X X, Wan C, Liu H, Li Z Q, Sheng P and Lin J J 2001 *Phys. Rev. Lett.* **86** 5562
[180] Wu Y N, Li Z Q and Lin J J 2011 *Phys. Rev.* B **82** 092202
[181] Wan C and Sheng P 2002 *Phys. Rev.* B **66** 075309
[182] Beloborodov I S, Lopatin A V, Schwiete G and Vinokur V M 2004 *Phys. Rev.* B **70** 073404
[183] Rotkina L, Oh S, Eckstein J N and Rotkin S V 2005 *Phys. Rev.* B **72** 233407
[184] Sachser R, Porrati F, Schwalb C H and Huth M 2011 *Phys. Rev. Lett.* **107** 206803
[185] Achatz P *et al* 2009 *Phys. Rev.* B **79** 201203
[186] Bakkali H and Dominguez M 2013 *Europhys. Lett.* **104** 17007
[187] Beloborodov I S, Lopatin A V and Vinokur V M 2004 *Phys. Rev.* B **70** 205120
[188] Glatz A and Beloborodov I S 2009 *Phys. Rev.* B **79** 041404
[189] Yeh S S, Hsu W M, Lee J K, Lee Y J and Lin J J 2013 *Appl. Phys. Lett.* **103** 123118